# 33

# INFRARED DETECTOR ARRAYS

## Lester J. Kozlowski

*Altasens, Inc.*
*Westlake Village, California*

## Walter F. Kosonocky*

*New Jersey Institute of Technology*
*University Heights*
*Newark, New Jersey*

## 33.1 GLOSSARY

| | |
|---|---|
| $A_{det}$ | detector area |
| $A_I$ | gate modulation current gain (ratio of integration capacitor current to load current |
| $A_V$ | amplifier voltage gain |
| $C_{amp}$ | amplifier capacitance |
| $C_{det}$ | detector capacitance |
| $C_{FIS}$ | fill-and-spill gate capacitance for a Tompsett type CCD input |
| $C_{fb}$ | CTIA feedback or Miller capacitance |
| $C_{gd}$ | FET gate-drain overlap capacitance |
| $C_{gs}$ | FET gate-source capacitance |
| $C_L$ | CTIA band-limiting load capacitance |
| $C_{out}$ | sense node capacitance at the CCD output |
| $C_T$ | effective feedback (transcapacitance) or integration capacitance for a capacitive transimpedance amplifier |
| $C_{T\lambda}$ | spectral photon contrast |
| cte | charge transfer efficiency |
| $D^*_{\lambda pk}$ | peak detectivity (cm-Hz$^{1/2}$/W or Jones) |
| $D^*_{bb}$ | blackbody detectivity (cm-Hz$^{1/2}$/W or Jones) |
| $D^*_{th}$ | thermal detectivity (cm-Hz$^{1/2}$/W or Jones) |
| e$^-$ | electron |
| $E_g$ | detector energy gap |
| $f/\#$ | conventional shorthand for the ratio of the focal length of a lens to its diameter |
| $f_{chop}$ | chopper frequency |

---

*Deceased.

**33.1**

| | |
|---|---|
| $f_{frame}$ | display frame rate |
| $f_{knee}$ | frequency at which the $1/f$ noise intersects the broadband noise |
| $f_s$ | spatial frequency (cycles/radian) |
| $g_{m,\,LOAD}$ | gate transconductance of the load FET in the gate-modulated input circuit |
| $g_m$ | gate transconductance of a Field Effect Transistor |
| $h$ | Planck's constant |
| $I_D$ | FET drain current |
| $I_{det}$ | detector current |
| $I_{photo}$ | detector photocurrent |
| $k$ | Boltzmann constant |
| $K_{amp}$ | amplifier FET noise spectral density at 1 Hz |
| $K_{det}$ | detector noise spectral density at 1 Hz |
| $K_{FET}$ | FET noise spectral density at 1 Hz |
| $L$ | length-to-width ratio of a bar chart (always set to 7) |
| MRT | minimum resolvable temperature (K) |
| MTF | modulation transfer function for the optics, detector, readout, the integration process, or the composite sensor |
| $n$ | detector junction ideality or diffusion constant |
| $N_{amp,\,1/f}$ | number of noise carriers for one integration time due to amplifier FET $1/f$ noise |
| $N_{amp,\,white}$ | number of noise carriers for one integration time due to amplifier FET white noise |
| $N_c$ | number of photo-generated carriers integrated for one integration time |
| $n_{det}$ | detector junction ideality or diffusion constant |
| NE $\Delta$T | noise equivalent temperature difference (K) |
| $n_{FET}$ | subthreshold FET ideality |
| $N_{FPA}$ | composite (total) FPA noise in carriers |
| $N_{kTC,\,channel}$ | CTIA broadband channel noise in carriers |
| $N_{load,\,white}$ | number of noise carriers for one integration time due to CTIA load FET white noise |
| $N_{os}$ | display overscan ratio |
| $N_{PHOTON}$ | shot noise of photon background in carriers |
| NSD | noise spectral density of a detector or field effect transistor; the $1/f$ noise is often specified by the NSD at a frequency of 1 Hz |
| $N_{sf}$ | source follower noise |
| $N_{ss}$ | serial scan ratio |
| $q$ | electron charge in coulombs |
| $Q_B$ | photon flux density (photons/cm$^2$-s) incident on a focal plane array |
| $Q_D$ | charge detected in a focal plane array for one integration time |
| $Q_{max}$ | maximum charge signal at saturation |
| $R_{det}$ | detector resistance |
| $R_{LOAD}$ | gate modulation load resistance |
| $R_0$ | detector resistance at zero-bias resistance |
| $R_0A$ | detector resistance-are product at zero-bias voltage |
| $R_r$ | detector resistance in reverse-bias resistance |
| S/N | signal-to-noise ratio |
| $SNR_T$ | target signal-to-noise ratio |
| $S_V$ | readout conversion factor describing the ratio of output voltage to detected signal carriers |
| $T$ | operating temperature |

| | |
|---|---|
| tce | thermal coefficient of expansion |
| TCR | thermal coefficient of resistance for bolometer detectors |
| $T_D$ | time constant for correlated double sampling process normally set by Nyquist rate |
| $t_{int}$ | integration time |
| $U$ | residual nonuniformity |
| $V_{br}$ | detector reverse-bias breakdown voltage, sometimes defined as the voltage where $R_r = R_0$ |
| $V_D$ | FET drain voltage |
| $V_{det}$ | detector bias voltage |
| $V_{DS}$ | FET grain-to-source voltage |
| $V_G$ | FET gate voltage |
| $v_n$ | measured rms noise voltage |
| $\Delta A_I$ | gate modulation current gain nonuniformity |
| $\Delta f$ | noise bandwidth (Hz) |
| $\Delta I_{photo}$ | differential photocurrent |
| $\Delta T$ | scene temperature difference creating differential photocurrent $\Delta I_{photo}$ |
| $\Delta V_S$ | signal voltage for differential photocurrent $\Delta I_{photo}$ |
| $\Delta x$ | horizontal detector subtense (mradian) |
| $\Delta y$ | vertical detector subtense (mradian) |
| $\eta$ | detector quantum efficiency |
| $\eta_{BLIP}$ | percentage of BLIP |
| $\eta_{inj, DI}$ | injection efficiency of detector current into the source-modulated FET of the direct injection input circuit |
| $\eta_{inj}$ | injection efficiency of detector current |
| $\eta_{noise}$ | injection efficiency of DI circuit noise into integration capacitor |
| $\eta_{pc}$ | quantum efficiency of photoconductive detector |
| $\eta_{pv}$ | quantum efficiency of photovoltaic detector |
| $\lambda_c$ | detector cutoff wavelength (50 percent of peak response, µm) |
| $\sigma_{det}$ | noise spectral density of total detector noise including photon noise |
| $\sigma_{input, ir}$ | noise spectral density of input-referred input circuit noise |
| $\sigma_{LOAD}$ | noise spectral density of input-referred load noise |
| $\sigma_{mux, ir}$ | noise spectral density of input-referred multiplexer noise |
| $\sigma_{VT}$ | rms threshold voltage nonuniformity across an FPA |
| $\tau_{amp}$ | amplifier time constant (s) |
| $\tau_{eye}$ | eye integration time (s) |
| $\tau_o$ | optical transmission |
| $\omega$ | angular frequency (radians) |
| $\langle e_{amp} \rangle$ | buffer amplifier noise for buffered direct injection circuit |

## 33.2  INTRODUCTION

Infrared sensors have been available since the 1940s to detect, measure, and image the thermal radiation emitted by all objects. Due to advanced detector materials and microelectronics, large scanning and staring focal plane arrays (FPA) with few defects are now readily available in the short wavelength infrared (SWIR; 1 to 3 µm), medium wavelength infrared (MWIR; ≈3 to 5 µm), and long wavelength infrared (LWIR; ≈8 to 14 µm) spectral bands. We discuss in this chapter the disparate FPA technologies, including photon and thermal detectors, with emphasis on the emerging types.

IR sensor development has been driven largely by the military. Detector requirements for missile seekers and forward looking infrared (FLIR) sensors led to high-volume production of photoconductive (PC) HgCdTe arrays starting in the 1970s. Though each detector requires direct connection to external electronics for purposes of biasing, signal-to-noise ratio (SNR) enhancement via time delay integration (TDI), and signal output, the first-generation FPAs displaced the incumbent Pb-salt (PbS, PbSe) and Hg-doped germanium devices, and are currently being refined using custom analog signal processing,[1] laser-trimmed solid-state preamplifiers, etc.

Size and performance limitations of first-generation FLIRs necessitated development of self-multiplexed FPAs with on-chip signal processing. Second-generation thermal imaging systems use high-density FPAs with relatively few external connections. Having many detectors that integrate longer, low-noise multiplexing and on-chip TDI (in some scanning arrays), second-generation FPAs offer higher performance and design flexibility. Video artifacts are suppressed due to the departure from ac-coupling and interlaced raster scan, and external connections are minimized. Fabricated in monolithic and hybrid methodologies, many detector and readout types are used in two basic architectures (staring and scanning). In a monolithic FPA, the detector array and the multiplexing signal processor are integrated in a single substrate. The constituents are fabricated on separate substrates and interconnected in a hybrid FPA.

FPAs use either photon or thermal detectors. Photon detection is accomplished using intrinsic or extrinsic semiconductors and either photovoltaic (PV), photoconductive (PC), or metal insulator semiconductor (MIS) technologies. Thermal detection relies on capacitive (ferro- and pyroelectric) or resistive bolometers. In all cases, the detector signal is coupled into a multiplexer and read out in a video format.

## Infrared Applications

Infrared FPAs are now being applied to a rapidly growing number of civilian, military, and scientific applications such as industrial robotics and thermography (e.g., electrical and mechanical fault detection), medical diagnosis, environmental and chemical process monitoring, Fourier transform IR spectroscopy and spectroradiometry, forensic drug analysis, microscopy, and astronomy. The combination of high sensitivity and passive operation is also leading to many commercial uses. The passive monitoring provided by the addition of infrared detection to gas chromatography-mass spectroscopy (GC-MS), for example, yields positive chemical compound and isomer detection without sample alteration. Fusing IR data with standard GC-MS aids in the rapid discrimination of the closely related compounds stemming from drug synthesis. Near-IR (0.7 to 0.1 μm) and SWIR spectroscopy and fluorescence are very interesting near-term commercial applications since they pave the way for high-performance FPAs in the photochemical, pharmaceutical, pulp and paper, biomedical, reference quantum counter, and materials research fields. Sensitive atomic and molecular spectroscopies (luminescence, absorpion, emission, and Raman) require FPAs having high quantum efficiency, low dark current, linear transimpedance, and low read noise.

## Spectral Bands

The primary spectral bands for infrared imaging are 3 to 5 and 8 to 12 μm because atomspheric transmission is highest in these bands. These two bands, however, differ dramatically with respect to contrast, background signal, scene characteristics, atmospheric transmission under diverse weather conditions, and optical aperture constraints. System performance is a complex combination of these and the ideal system requires dual band operation. Factors favoring the MWIR include its higher contrast, superior clear-weather performance, higher transmissivity in high humidity, and higher resolution due to ~3 × smaller optical diffraction. Factors favoring the LWIR include much-reduced background clutter (solar glint and high-temperature countermeasures including fires and flares have much-reduced emission), better performance in fog, dust, and winter haze, and higher immunity to atmospheric turbulence. A final factor favoring the LWIR, higher

S/N ratio due to the greater radiance levels, is currently moot because of technology limitations. Due to space constraints and the breadth of sensor applicability, we focus on target/background metrics in this section.

The signal collected by a visible detector has higher daytime contrast than either IR band because it is mainly radiation from high-temperature sources that is subsequently reflected off earth-based (ambient temperature; ≈290 K) objects. The high-temperature sources are both solar (including the sun, moon, and stars) and synthetic. Since the photon flux from high- and low-temperature sources differs greatly at visible wavelengths from day to night, scene contrasts of up to 100 percent ensue.

Reflected solar radiation has less influence as the wavelength increases to a few microns since the background radiation increases rapidly and the contrast decreases. In the SWIR band, for example, the photon flux density from the earth is comparable to visible room light ($10^{13}$ photons/cm²-s). The MWIR band ($\sim 10^{15}$ photon flux density) has lower, yet still dynamic, daytime contrast, and can still be photon-starved in cold weather or at night.

The net contribution from reflected solar radiation is even lower at longer wavelengths. In the LWIR band, the background flux is equivalent to bright sunlight ($\approx 10^{17}$ photons/cm²-s). This band thus has even lower contrast and much less background clutter, but the "scene" and target/background metrics are similar day and night. Clear-weather performance is relatively constant.

Depending on environmental conditions, however, IR sensors operating in either band must discern direct emission from objects having temperatures very near the average background temperature (290 K) in the presence of the large background and degraded atmospheric transmissivity. Under conditions of uniform thermal soak, such as at diurnal equilibrium, the target signal stems from minute emissivity differences.

The spectral photon incidence for a full hemispheric surround is

$$Q = \tau_{cf} \int_{\lambda_1}^{\lambda_2} Q_\lambda(\lambda) d\lambda \tag{1}$$

if a zero-emissivity bandpass filter having in-band transmission $\tau_{cf}$, cut-on wavelength $\lambda_1$, and cutoff wavelength $\lambda_2$ is used (zero emissivity obtained practically by cooling the spectral filter to a temperature where its self-radiation is negligible). The photon flux density, $Q_B$ (photons/cm²-s), incident on a focal plane array is

$$Q_B = \frac{1}{4(f/\#)^2 + 1} Q \tag{2}$$

where $f/\#$ is the conventional shorthand for the ratio of the focal length to the diameter (assumed circular) of the limiting aperture or lens. The cold shield $f/\#$ limits the background radiation to a field-of-view consistent with the warm optics to eliminate extraneous background flux and concomitant noise. The background flux in the LWIR band is approximately two orders of magnitude higher than in the MWIR.

The spectral photon contrast, $C_{T\lambda}$, is the ratio of the derivative of spectral photon incidence to the spectral photon incidence, has units $K^{-1}$, and is defined

$$C_{T\lambda} = \left( \frac{\frac{\partial Q}{\partial T}}{Q} \right) \tag{3}$$

Figure 1 is a plot of $C_{T\lambda}$ for several MWIR subbands (including 3.5 to 5, 3.5 to 4.1, and 4.5 to 5 μm) and the 8.0 to 12 μm LWIR spectral band. The contrast in the MWIR bands at 300 K is 3.5 to 4 percent compared to 1.6 percent for the LWIR band. While daytime MWIR contrast is even higher due to reflected sunlight, an LWIR FPA offers higher sensitivity if it has the larger capacity needed for storing the larger amounts of photogenerated (due to the higher background flux) and detector-generated carriers (due to the narrow bandgap). The photon contrast and the background flux are key parameters that determine thermal resolution as will be described later under "Performance Figures of Merit."
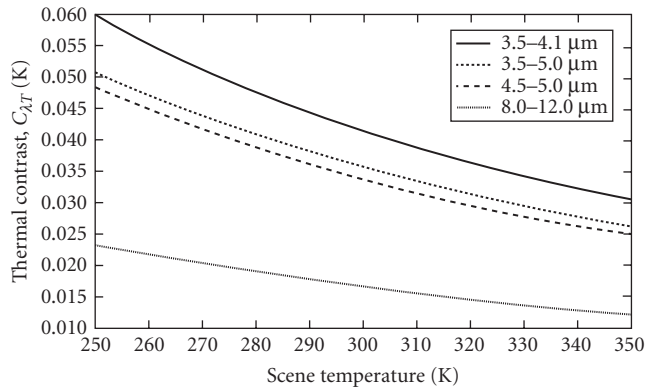
**FIGURE 1**    Spectral photon contrast in the MWIR and LWIR.

## Scanning and Staring Arrays

The two basic types of FPA are scanning and staring. The simplest scanning device consists of a linear array as shown in Fig. 2a. An image is generated by scanning the scene across the strip. Since each detector scans the complete horizontal field-of-view (one video raster line) at standard video frame rates, each resolution element or pixel has a short integration time and the total detected charge can usually be accommodated.

A staring array (Fig. 2b) is the two-dimensional extension of a scanning array. It is self-scanned electronically, can provide enhanced sensitivity, and is suitable for lightweight cameras. Each pixel
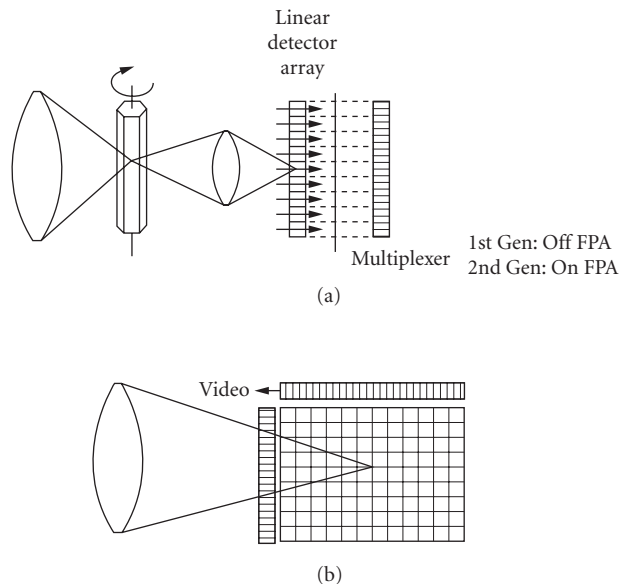


**FIGURE 2**    Scanning (*a*) and staring (*b*) focal plane arrays.

is a dedicated resolution element, but synchronized dithering of sparsely populated arrays is sometimes used to enhance the effective resolution, minimize spatial aliasing, and increase the effective number of pixels. Although theoretically charge can be integrated for the full frame time, the charge-handling capacity is inadequate at terrestrial LWIR backgrounds.

## Detectors

Infrared detectors convert IR photons and energy to electrical signals. Many types are used in FPAs (as shown in Fig. 3[2]) including photon and thermal detectors that address diverse requirements spanning operating temperatures from 4 K to room temperature. Figure 4 compares the quantum efficiencies of several detector materials.

Intrinsic detectors[3] usually operate at higher temperatures than extrinsic devices, have higher quantum efficiencies, and dissipate less power. Backside-illuminated devices, consisting of an absorbing epitaxial layer on a transparent substrate, are used in hybrid FPAs and offer the advantages of nearly 100 percent active detector area, good mechanical support, and high quantum efficiency. The most popular intrinsic photovoltaics are HgCdTe and InSb. These detectors are characterized by their quantum efficiency ($\eta$), zero-bias resistance ($R_0$), reverse-bias resistance ($R_r$), junction ideality or diffusion constant $n$, excess noise (if any) versus bias, and reverse-bias breakdown voltage ($V_{br}$), which is sometimes defined as the voltage where $R_r = R_0$.

PtSi is a photovoltaic Schottky barrier detector (SBD) which is the most mature for large monolithic FPAs. IR detection is via internal photoemission over a Schottky barrier (0.21 to 0.23 eV). Characteristics include low ($\approx 0.5$ percent for broadband 3.5 to 5.0 µm) but very uniform quantum efficiency, high producibility that is limited only by the Si readout circuits, full compatibility with VLSI technology, and soft spectral response with peak below 2 µm and zero response just beyond 6 µm. Internal photoemission dark current requires cooling below 77 K.

HgCdTe is the most popular intrinsic photoconductor, and various linear arrays in several scanning formats are used worldwide in first-generation FLIRs. For reasons of producibility and cost, HgCdTe photoconductors have historically enjoyed a greater utilization than PV detectors despite the latter's higher quantum efficiency, higher $D^*$ by a factor of $(2\eta_{pv}/\eta_{pc})^{1/2}$, and superior modulation transfer function (MTF). Nevertheless, not all photoconductors are good candidates for FPAs due to their low detector impedance. This includes the intrinsic materials InSb and HgCdTe.

The most popular photoconductive material system for area arrays is doped extrinsic silicon (Si: $x$; where $x$ is In, As, Ga, Sb, etc.), which is made in either conventional or impurity band conduction [IBC or blocked impurity band (BIB)] technologies. Early monolithic arrays were doped-Si devices, due primarily to compatibility with the silicon readout. Extrinsic photoconductors must be made relatively thick (up to 30 mils; doping density of IBCs, however, minimizes this thickness requirement but does not eliminate it) because they have much lower photon capture cross section than intrinsic detectors. This factor adversely affects their MTF in systems having fast optics.

Historically, Si:Ga and Si:In were the first mosaic focal plane array PC detector materials because early monolithic approaches were compatible with these dopants. Nevertheless, problems in fabricating the detector contacts, early breakdown between the epitaxial layer and the detector material (double injection), and the need for elevated operating temperatures helped force the general move to monolithic PtSi and intrinsic hybrids.

The most advanced extrinsic photoconductors are IBC detectors using Si:As and Si:Ga.[4] These have reduced recombination noise (negating the $\sqrt{2}$ superiority in S/N that PV devices normally have) and longer spectral response than standard extrinsic devices due to the higher dopant levels. IBC detectors have a unique combination of PC and PV characteristics, including extremely high impedance, PV-like noise (reduced recombination noise since IBC detectors collect carriers both from the continuum and the "hopping" impurity band), linear photoconductive gain, high uniformity, and superb stability. The photo-sensitive layer in IBCs is heavily doped to achieve hopping-type conduction. A thin, lightly doped ($10^{10}/cm^2$) silicon layer blocks the hopping current before
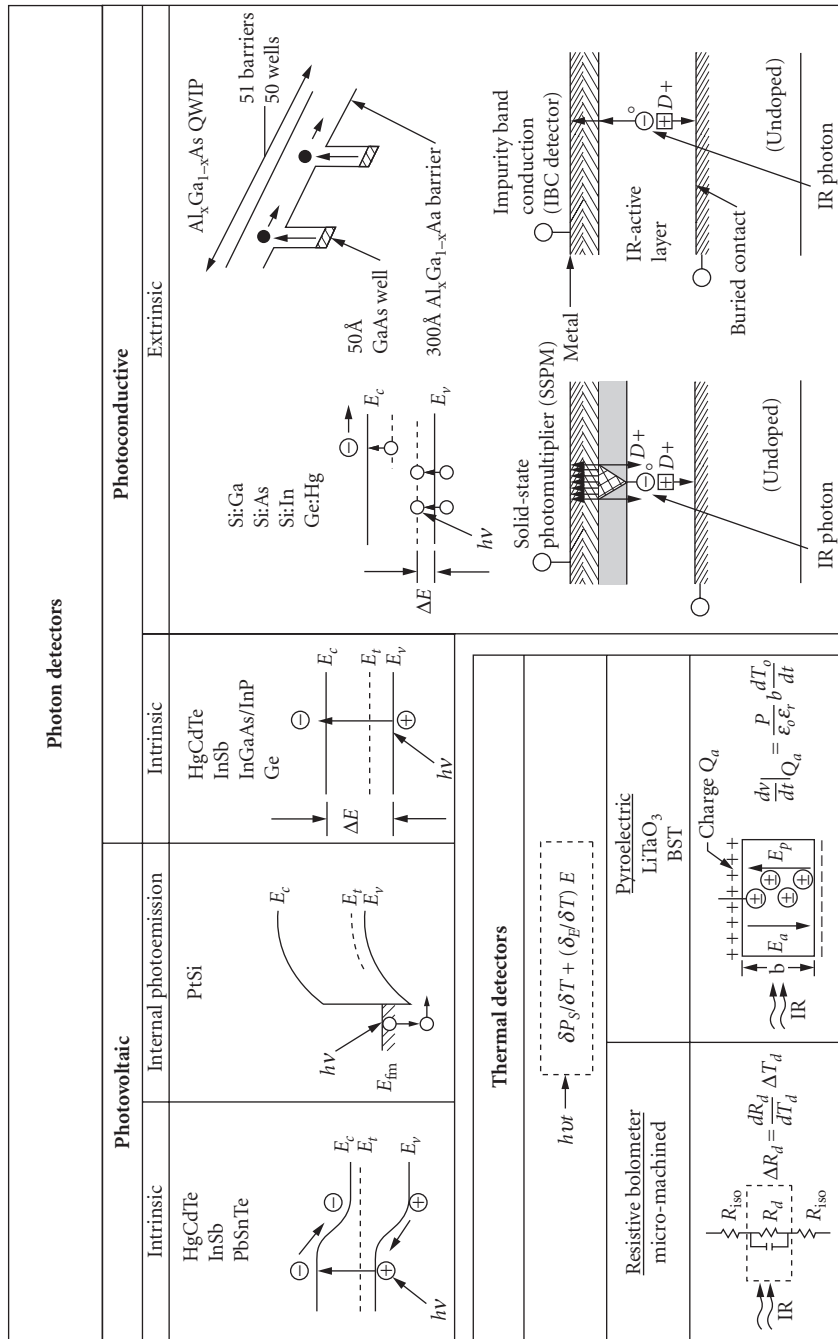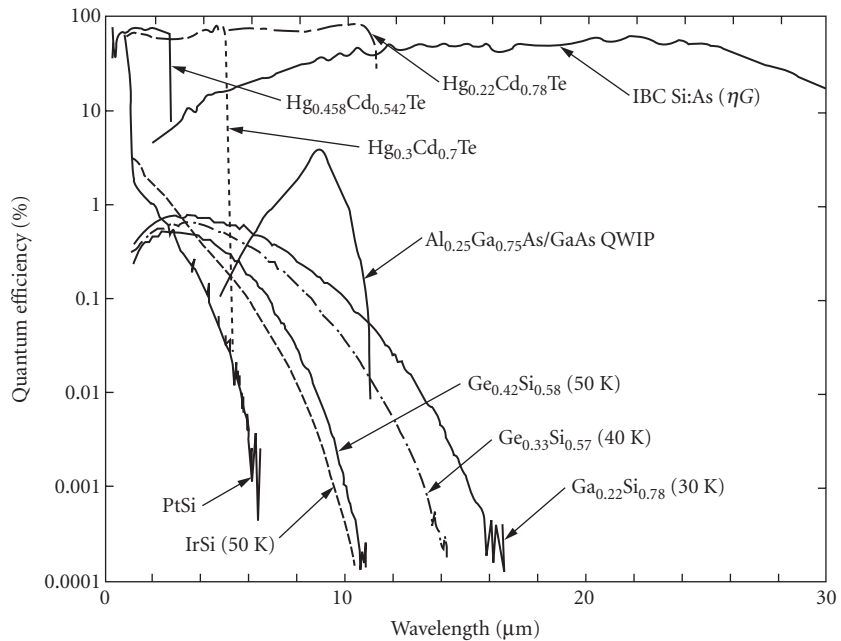
**33.8**



**FIGURE 3** Photon and thermal detectors.

**FIGURE 4**    Quantum efficiency versus wavelength for several detector materials.

it reaches the device electrode to reduce noise. Specially doped IBCs (see cross-sectional views in Fig. 3) operate as solid-state photomultipliers (SSPM) and visible light photon counters (VLPC) in which photoexcited carriers are amplified by impact ionization of impurity-bound carriers.[5] The amplification allows counting of individual photons at low flux levels. Standard SSPMs respond from 0.4 to 28 μm.

An alternative custom tunable detector is the GaAs/AlGaAs quantum well infrared photodetector (QWIP). Various QWIP photoconductive[6] and photovoltaic[7] structures are being investigated as low-cost alternatives to II-VI LWIR detectors like HgCdTe. Infrared detection in the typical PC QWIP is via intersubband or bound-to-extended-state transitions within the multiple quantum well superlattice structure. Due to the polarization selection rules for transitions between the first and second quantum wells, the photon electric field must have a component parallel to the superlattice direction. Light absorption in *n*-type material is thus anisotropic with zero absorption at normal incidence. The QWIP detector's spectral response is narrowband, peaked about the absorption energy. The wavelength of peak response can be adjusted via quantum well parameters and can be made bias-dependent.

Various bolometers, both resistive and capacitive (pyroelectric), are also available. Bolometers sense incident radiation via energy absorption and concomitant change in device temperature in both cooled moderate-performance and uncooled lower-performance schemes. Much recent research, which was previously highly classified, has focused on both hybrid and monolithic uncooled arrays and has yielded significant improvements in the detectivity of both resistive and capacitive bolometer arrays. The resistive bolometers currently in development consist of a thin film of a temperature-sensitive resistive material film which is suspended above a silicon readout. The pixel support struts provide electrical interconnect and high thermal resistance to maximize pixel sensitivity. Recent work has focused on the micromachining necessary to fabricate mosaics with low thermal conductance using monolithic methodologies compatible with silicon.

Capacitive bolometers sense a change in elemental capacitance and require mechanical chopping to detect incident radiation. The most common are pyroelectric detectors. J. Cooper[8] suggested the use of pyroelectric detectors in 1962 as a possible solution for applications needing a low-cost IR FPA with acceptable performance. These devices have temperature-dependent spontaneous polarization. Ferroelectric detectors are pyroelectric detectors having reversible polarization. There are over a thousand pyroelectric crystals, including several popularly used in hybrid FPAs; e.g. lithium tantalate ($LiTaO_3$), triglycine sulfate (TGS), and barium strontium titanate[9] ($BaSrTiO_3$).

## 33.3  MONOLITHIC FPAs

A monolithic FPA consists of a detector array and the readout multiplexer integrated on the same substrate. The progress in the development of the monolithic FPAs in the last two decades has been strongly influenced by the rapid advances in the silicon VLSI technology. Therefore, the present monolithic FPAs can be divided into three categories reflecting their relationship to the silicon VLSI technology. The first category includes the "complete" monolithic FPAs in which the detector array and the readout multiplexer are integrated on the same silicon substrate using processing steps compatible with the silicon VLSI technology. They include the extrinsic Si FPAs reported initially in the 1970s,[10] FPAs with Schottky barrier,[11] heterojunction detector FPAs, and microbolometer FPAs.[12]

The second category will be referred to here as the "partial monolithic" FPAs. This group includes narrowband detector arrays of HgCdTe[13] and InSb[14] integrated on the same substrate only with the first level of multiplexing, such as the row and column readout from a two-dimensional detector array. In this case the multiplexing of the detected signal is completed by additional silicon IC chips usually packaged on the imager focal plane.

The third category represents "vertically integrated" photodiode (VIP) FPAs. These FPAs are functionally similar to hybrids in the sense that a silicon readout multiplexer is used with the narrowbandgap HgCdTe detectors. However, while in the hybrid FPA the completed HgCdTe detector array is typically connected by pressure contacts via indium bumps to the silicon multiplex pads; in the case of the vertically integrated FPAs, HgCdTe chips are attached to a silicon multiplexer wafer and then the fabrication of the HgCdTe photodiodes is completed including the deposition and the definition of the metal connections to the silicon readout multiplexer.

In the following sections we will review the detector readout structures, and the main monolithic FPA technologies. It should also be noted that most of the detector readout techniques and the architectures for the monolithic FPAs were originally introduced for visible silicon imagers. This heritage is reflected in the terminology used in the section.

### Architectures

The most common structures for the photon detector readout and architectures of monolithic FPAs are illustrated schematically in Figs. 5 and 6.

*MIS Photogate FPAs: CCD, CID, and CIM*   Most of the present monolithic FPAs use either MIS photogates or photodiodes as the photon detectors. Figure 5 illustrates a direct integration of the detected charge in the potential well of a MIS (photogate) detector for a charge coupled device (CCD) readout in (*a*), a charge injection device (CID) readout in (*b*), and a charge-integration matrix (CIM) readout in (*c*). The unique characteristic of the CCD readout is the complete transfer of charge from the integration well without readout noise. Also in a CCD FPA the detected charge, $Q_D$, can be transferred via potential wells along the surface of the semiconductor that are induced by clock voltages but isolated from the electrical pickup until it is detected by a low-capacitance (low kTC noise) on-chip amplifier. However, because of the relatively large charge transfer losses ($\sim 10^{-3}$ per transfer) and a limited charge-handling capacity, the use of nonsilicon CCD readout has
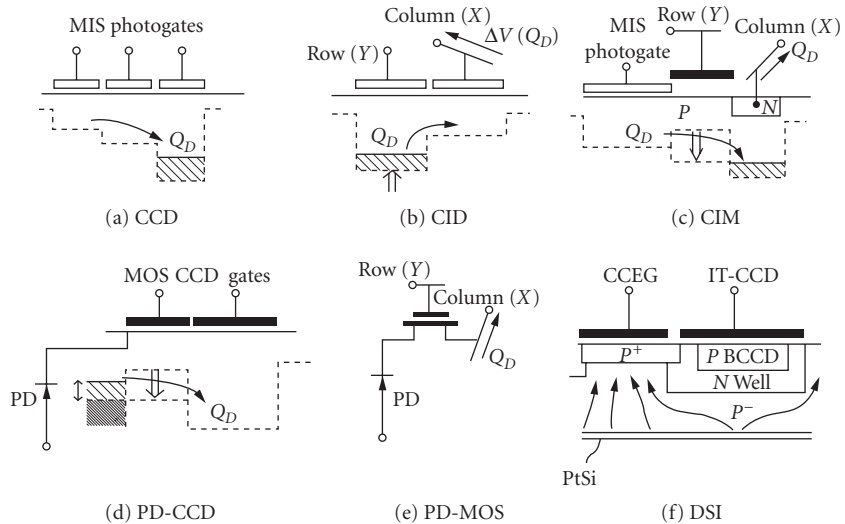
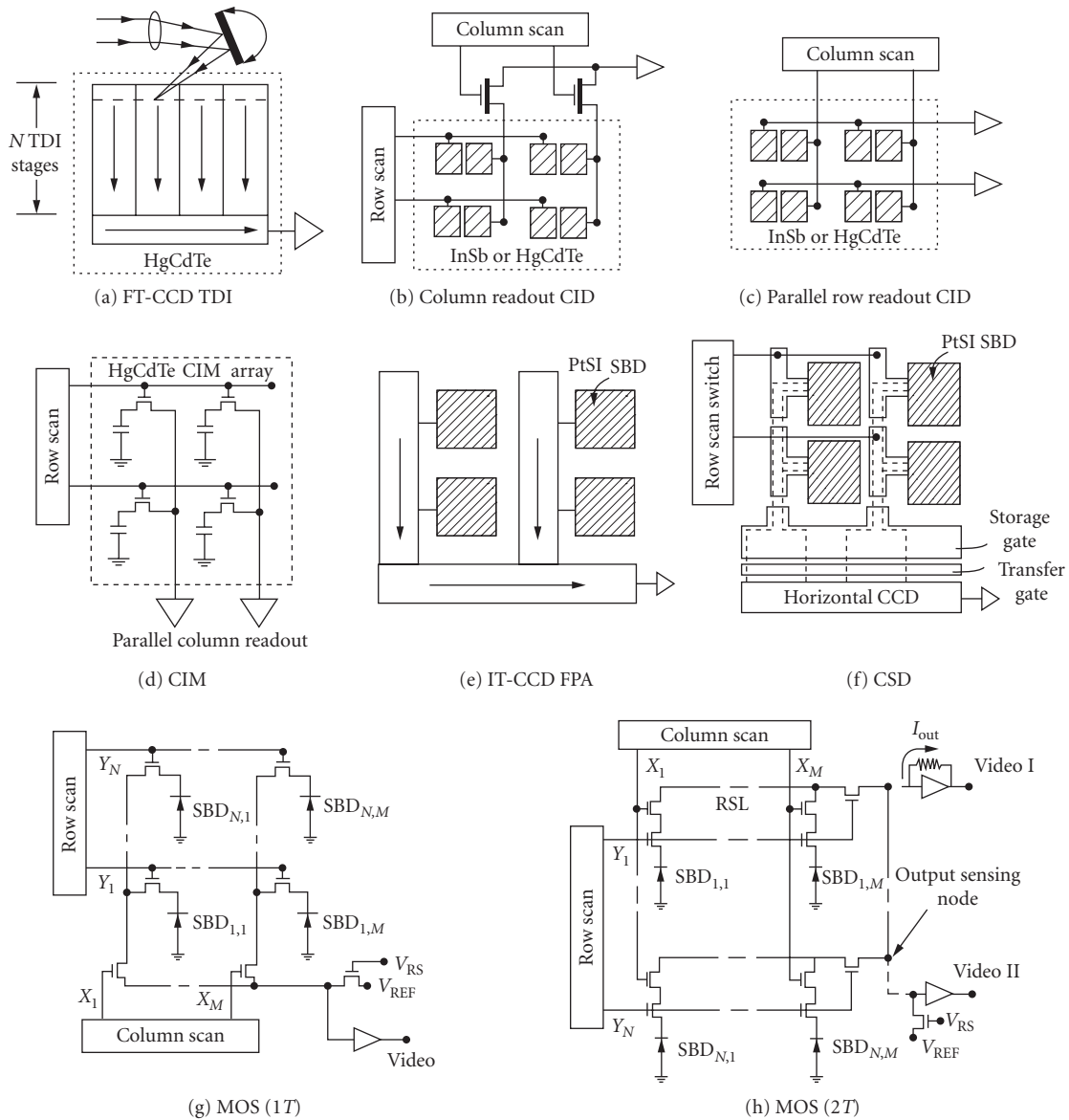**FIGURE 5**    Photodetector readout structures.

been limited mainly to HgCdTe TDI FPAs. Such TDI imager is shown in Fig. 6a as a frame transfer (FT) type CCD area imager performing a function of a line sensor with the effective optical integration time increased by the number of TDI elements (CCD stages) in the column CCD registers. In this imager the transfer of the detected charge signal between CCD wells of the vertical register is adjusted to coincide with the mechanical motion of the image.

In the FT-CCD TDI FPA, the vertical registers perform the functions of charge detection and integration as well as transfer. The detected image is transferred one line at a time from the parallel vertical registers to the serial output registers. From there it is transferred at high clock rate to produce the output video. Similar TDI operation can also be produced by the interline-transfer (IT) CCD architecture shown in Fig. 6e. However, in the case of IT-CCD readout, the conversion of infrared radiation into charge signal photodetection is performed by photodiodes.

In the CID readout, see Fig. 5b, the detected charge signal is transferred back and forth between the potential wells of the MIS photogates for nondestructive X-Y addressable readout, $\Delta V(Q_D)$, that is available at a column (or a row) electrode due to the displacement current induced by the transfer of the detected charge signal, $Q_D$. At the end of the optical integration time, the detected charge is injected into the substrate by driving both MIS capacitors into accumulation.

CID FPAs with column readout for single-output-port and parallel-row readout are illustrated schematically in Fig. 6b and c, respectively. Another example of a parallel readout is the CIM FPA shown in Fig. 6d. The parallel readout of CID and CIM FPAs is used to overcome the inherent limitation on charge-handling capacity of these monolithic FPAs by allowing a short optical integration time with fast frame readout and off-chip charge integration by supporting silicon ICs.

***Silicon FPAs: IT-CCD, CSD, and MOS FPAs***    The monolithic FPAs fabricated on silicon substrate take advantage of well-developed silicon VLSI process technology. Therefore, silicon $(E_g = 1.1$ eV), which is transparent to infrared radiation having wavelength longer than 1.0 μm, is often used to produce monolithic CCD and MOS FPAs with infrared detectors that can be formed on silicon substrate. In the 1970s there was great interest in the development of monolithic silicon FPAs with extrinsic Si:In and Si:Ga photoconductors. However, since the early 1980s most progress was reported on monolithic FPAs with Schottky-barrier photodiodes, GeSi/Si heterojunction photodiodes, vertically integrated photodiodes, and resistive microbolometers. With the exception of the

(a) FT-CCD TDI

(b) Column readout CID

(c) Parallel row readout CID

(d) CIM

(e) IT-CCD FPA

(f) CSD

(g) MOS (1$T$)

(h) MOS (2$T$)

**FIGURE 6**    Monolithic FPA architectures.

resistive microbolometers, in the form of thin-film semiconductor photoresistors formed on micro-machined silicon structures, all of the above infrared detectors can be considered to be photodiodes and can be read out either by IT-CCD or MOS monolithic multiplexer.

The photodiode (PD) CCD readout, see Fig. 5$d$, is normally organized as the interline-transfer (IT) CCD staring FPA, shown in Fig. 6$e$. The IT-CCD readout has been used mostly for PtSi Schottky-barrier detectors (SBDS). The operation of this FPA consists of direct integration of the detected charge signal on the capacitance of the photodiode. At the end of the optical integration time, a frame readout is initiated by a parallel transfer of the detected charge from the photodiodes to the

parallel vertical CCD registers. From there the detected image moves by parallel transfers one line at a time into the horizontal output register for a high-clock-rate serial readout.

The design of the Schottky-barrier IT-CCD FPA involves a trade-off between fill factor (representing the ratio of the active detector area to the pixel area) and maximum saturation charge signal ($Q_{mix}$). This trade-off can be improved by the charge sweep device (CSD) architecture, shown in Fig. 6f, that has also been used as a monolithic readout multiplexer for PtSi and IrSi SBDs.

In CSD FPA the maximum charge signal is limited only by the SBD capacitance since its operation is based on transferring the detected charge signal from one horizontal line corresponding to one or two rows of SBDs (depending on the type of the interlacing used) into minimum geometry vertical CCD registers. During the serial readout of the previous horizontal line, the charge signal is swept into a potential well under the storage gate by low-voltage parallel clocking of the vertical registers. Then, during the horizontal blanking time, the line charge signal is transferred in parallel to the horizontal CCD register for serial readout during the next horizontal line time.

The main advantage of the silicon CCD multiplexer is relatively low readout noise, from a few electrons to the order of several tens of electrons (depending on video rate, sense capacitance, and CCD technology), so that a shot-noise-limited operation can be achieved at relatively low signal levels. But as the operating temperature is lowered below 60 K, the charge transfer losses of buried-channel CCDs (BCCDs) become excessive due to the freeze-out of the BCCD implant. Therefore, detectors requiring operation at 40 K or lower are more compatible with MOS readout device technology.

Photodiode (PD) MOS readout (see Fig. 5e) represents another approach to construction of an X-Y addressable silicon multiplexer. These types of monolithic MOS multiplexers used for readout of PtSi SBDs are illustrated in Fig. 6g and h.

A single-output-port FPA with one MOSFET switch per detector, MOS (1T), is shown in Fig. 6g. During FPA readout, the vertical scan switch transfers the detected charge signal from one row of detectors to the column lines. Then the column lines are sequentially connected by MOSFET switches to the output sense line under the control of the horizontal scan switch. The main limitation of the MOS (IT) FPA is a relatively high readout noise (on the order of 100 electrons/pixel) due to sensing of small charge signals on large-capacitance column lines. This readout noise can be decreased with a row readout MOS (2T) FPA having two MOSFET switches per detector. In this case, low readout noise can be achieved using current sensing, it is limited by the noise of the amplifier, and for voltage sensing it can be reduced by correlated double sampling (CDS).[15] A readout noise of 300 rms electrons/pixel was achieved at Sarnoff for a $640 \times 480$ low-noise PtSi MOS (2T) FPA designed with row buffers and 8:1 multiplexing of the output lines;[16] 2T MOS FPA read noise of $60e^-$ was later achieved by reading via capacitive transimpedance amplifier column buffers in 0.5 µm CMOS technology.[17]

An alternative form of the MOS (IT) FPA architecture is an MOS FPA with parallel column readout for fast frame operation. This silicon VIP FPA, resembling CIM architecture in Fig. 6d, can be used with HgCdTe vertically integrated PV detectors.

**Direct-Charge-Injection Silicon FPAs**    All of the silicon monolithic FPAs thus far described use separately defined detectors. A direct-charge-injection type monolithic silicon FPA with a single detector surface is a PtSi direct Schottky injection (DSI) imager that is made on thinned silicon substrate having a CCD or MOS readout on one side and PtSi SBD charge-detecting surface on the other side.[18] A cross-sectional area of one pixel of this FPA for IT-CCD readout is shown in Fig. 5f. In the operation of this imager, the p-type buried-channel CCD formed in an n-well removes charge from a $P^+$ charge-collecting electrode that in turn depletes a high-resistivity p-type substrate. Holes injected from the PtSi SBD surface into the p-type substrate drift through the depleted p-type substrate to the $P^+$ charge-collecting electrode. The advantages of the DSI FPA include 100 percent fill factor, a large maximum charge due to the large capacitance between the charge collecting electrode and the overlapping gate, and that the detecting surface does not have to be defined. A $128 \times 128$ IT-CCD PtSi DSI FPA was demonstrated;[19] however, the same basic structure could also be used with other internal photoemission surfaces such as IrSb or Ge:Si.

**Microbolometer FPAs**    A microbolometer FPA for uncooled applications consists of thin-film semiconductor photoresistors micromachined on a silicon substrate. The uncooled IR FPA is fabricated as an array of microbridges with a thermoresistive element in each microbridge. The

resistive microbolometers have high thermal coefficient of resistance (TCR) and low thermal conductance between the absorbing area and the readout circuit which multiplexes the IR signal. As each pixel absorbs IR radiation, the microbridge elemental resistance changes accordingly with its temperature.

Metal films have traditionally been used to make the best bolometer detectors because of their low 1/$f$ noise. These latest devices use semiconductor films of 500 Å thickness having TCR of 2 percent per °C. The spacing between the microbridge and the substrate is selected to maximize the pixel absorption in the 8- to 14-μm wavelength range. Standard photolithographic techniques pattern the thin film to form detectors for individual pixels. The thin film TCR varies over an array by ±1 percent, and produces responsivity of 70,000 V/W in response to 300 K radiation. This has been sufficient to yield 0.1°C NE $\Delta T$ with an $f$/1 lens. Potential low-cost arrays at prices similar to that of present large IC memories are possible with this technology.

## Scanning and Staring Monolithic FPAs

In an earlier section we have reviewed the available architectures for the construction of two-dimensional scanning TDI, scanning, and staring FPAs. The same basic readout techniques, however, are also used for line-sensing imagers with photodiodes and MIS photogate detectors. For example, a line-scanning FPA corresponds to a vertical column CCD with the associated photodiodes of an IT-CCD, a column readout CID, a MOS (IT) FPA with only one row of detectors. However, since the design of a staring FPA is constrained by the size of the pixels, there is more space available for the readout multiplexer of a line of detectors. Therefore, design of the monolithic silicon multiplexer for a line detector array may also resemble the complexity of silicon multiplexer for hybrid FPAs.

## 33.4  HYBRID FPAs

Hybrid FPAs are made by interconnecting, via either direct or indirect means, a detector array to a multiplexing readout. Several approaches are pursued in both two- and three-dimensional configurations. Hybrids are typically made by either epoxying detector material to a processed silicon wafer (or readout) and subsequently forming the detectors and electrical interconnects by, for example, ion-milling; by mating a fully processed detector array to a readout to form a "two-dimensional" hybrid;[20] or by mating a fully processed detector array to a stack of signal processors to form a three-dimensional stack ($Z$-hybrid or "3D-IC"). The detector is usually mounted on top of the multiplexer and infrared radiation impinges on the backside of the detector array. Indium columns typically provide electrical and, often in conjunction with various epoxies, mechanical interconnect.

Hybrid methodology allows independent optimization of the detector array and the readout. Silicon is the preferred readout material due to performance and the leveraging of the continuous improvements funded by commercial markets. Diverse state-of-the-art processes and lithography are hence available at a fraction of their original development cost.

*Thermal expansion match*    In a hybrid FPA, the detector array is attached to a multiplexer which can be of a different material. In cooling the device from room temperature to operating temperature, mechanical strain builds up in the hybrid due to the differing coefficients of thermal expansion. Hybrid integrity requires detector material that has minimum thermal expansion mismatch with silicon. Based on this criterion, the III-V and II-VI detectors are favored over Pb-salts. Silicon-based detectors are matched perfectly to the readout; these include doped-Si and PtSi. The issue of hybrid reliability has prompted the fabrication of II-VI detectors on alternative substrates to mitigate the mismatch. HgCdTe, for example, is being grown on sapphire (PACE-I),[21] GaAs (liftoff techniques are available for substrate thinning or removal), and silicon in addition to the lattice-matched Cd(Zn)Te substrates. Detector growth techniques[22] include liquid phase epitaxy and vapor phase epitaxy (VPE). The latter includes metal organic chemical vapor deposition (MOCVD) and molecular beam epitaxy (MBE).

## Hybrid Readout

Hybrid readouts perform the functions of detector interface, signal processing, and video multiplexing.[23] The hybrid FPA readout technologies include

- Surface channel charge coupled device (SCCD)
- Buried channel charge coupled device (BCCD)
- *x-y* addressed switch-FET (SWIFET) or direct readout (DRO) FET arrays
- Combination of MOSFET and CCD (MOS/CCD)
- Charge-injection device (CID)

Early hybrid readouts were either CIDs[24] or CCDs, and the latter are still popular for silicon monolithics. However, *x-y* arrays of addressed MOSFET switches are superior for most hybrids for reasons of yield, design flexibility, simplified interface, and direct leveraging of Moore's Law for ongoing improvements and cost reduction. The move to the FET-based, direct readouts is key to the dramatic improvements in staring array producibility and is a consequence of the spin-off benefits from the silicon memory markets. DROs are fabricated with high yield and are fully compatible with advanced processes that are available at captive and commercial foundries. We will thus focus our discussion on these families. Though not extensively, CCDs are still sometimes used in hybrid FPAs.[25]

*Nonsilicon readouts*     Readouts have been developed in Ge, GaAs, InSb, and HgCdTe. The readout technologies include monolithic CCD, charge-injection device (CID), charge-injection matrix (CIM), enhancement/depletion (E/D) MESFET (GaAs), complementary heterostructure FET (C-HFET; GaAs),[26] and JFET (GaAs and Ge). The CCD, CID, and CIM readout technologies generally use MIS detectors for monolithic photon detection and signal processing.

The CID and CIM devices rely on accumulation of photogenerated charge within the depletion layer of a MIS capacitor that is formed using a variety of passivants (including CVD and photo-$SiO_2$, anodic $SiO_2$, and ZnS). A single charge transfer operation then senses the accumulated charge. Device clocking and signal readout in the CIDs and CIMs relies on support chips adjacent to the monolithic IR FPA. Thus, while the FPA is monolithic, the FPA assembly is actually a multichip hybrid.

CCDs have been demonstrated in HgCdTe and GaAs.[27] The *n*-channel technology is preferred in both materials for reasons of carrier mobility and device topology. In HgCdTe, for example, *n*-MOSFETs with CVD $SiO_2$ gate dielectric have parametrics that are in good agreement with basic silicon MOSFET models. Fairly elaborate circuits have been demonstrated on CCD readouts, e.g., an on-chip output amplifier containing a correlated double sampler (CDS).

GaAs has emerged as a material that is very competitive for niche applications including IR FPAs. Since GaAs has very small thermal expansion mismatch with many IR detector materials including HgCdTe and InSb, large hybrids are possible, and VPE detector growth capability suggests future development of composite monolithic FPAs. The heterostructure (H-)MESFET and C-HFET technologies are particularly interesting for IR FPAs because low 1/*f* noise has been demonstrated; noise spectral densities at 1 Hz of as low as 0.5 $\mu$V/$\sqrt{Hz}$ for *p*-HIGFET and 2 $\mu$V/$\sqrt{Hz}$ for the enhancement H-MESFET[28] at 77 K have been achieved. The H-MESFET has the advantage of greater fabrication maturity (16 K SRAM and 64 $\times$ 2 readout demonstrated), but the C-HFET offers lower power dissipation.

*Direct Readout Architectures*     The DRO multiplexer consists of an array of FET switches. The basic multiplexer has several source follower stages that are separated at the cell, row, and column levels by MOSFET switches which are enabled and disabled to perform pixel access, reset, and multiplexing. The signal voltage from each pixel is thus direct-coupled through the cascaded source follower architecture as shown, for example, in Fig. 7. Shift registers generate the various clock signals; a minimum of externally supplied clocks is required. Since CMOS logic circuitry is used, the clock levels do not require precise adjustment for optimum performance. The simple architecture also gives high functional yield even in readout materials less mature than silicon.
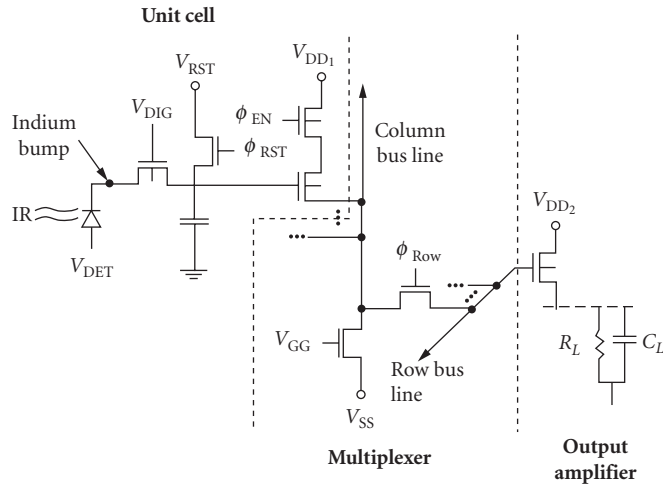
**FIGURE 7**   Direct readout schematic (shown with direct injection input).

Owing to the relatively low internal impedances beyond the input circuit, multiplexer noise is usually negligible. The inherent dynamic range is often >100 dB and the FPA dynamic range is limited only by the output-referred noise of the input circuit and the maximum signal excursion. The minimum read noise for DROs in imaging IR FPAs is typically capacitor reset noise. Correlated double samplers are thus used to suppress the reset noise for highest possible SNR at low integrated signal level.

In addition to excellent electrical characteristics, the DRO has excellent electro-optical properties including negligible MTF degradation and no blooming. Crosstalk in DRO-based FPAs is usually detector-limited since the readouts typically have low (<0.005 percent) electrical crosstalk. DROs also have higher immunity to clock feedthrough noise due to their smaller clock capacitances. Substrate charge pumping, which causes significant FET backgating[29] and transconductance degradation in SCCDs, is low in DROs.

*X-Y addressing and clock generation*   Both static and dynamic shift registers are used to generate the clock signals needed for cell access, reset, and pixel multiplexing. Static registers offer robust operation and increased hardness to ionizing radiation in trade for increased FET count and preference for CMOS processes. Dynamic registers use fewer transistors in NMOS or PMOS processes, but require higher voltages, have lower maximum clocking rate, and must be carefully designed to avoid being affected by incident radiation.

Dynamic shift registers use internal bootstrapping to regenerate the voltage at each tap. The circuit techniques limit both the lowest and highest clock rates and require fine-tuning of the MOSFET design parameters for the specific operating frequency. More importantly, the high internal voltages stress conventional CMOS processes.

*Electronically scanned staring FPAs*   The inability to integrate photogenerated charge for full staring frame times is often handled by integration time management. Since the photon background for the full 8- to 12-μm spectral band is over two orders of magnitude larger than the typical MWIR passband, and since the LWIR detector dark current is several orders of magnitude larger than similarly sized MWIR devices, LWIR FPA integration duty cycle can be quite poor. It is sometimes prudent to concede the limited duty cycle by electronically scanning the staring readout. Electronic scanning refers to a modified staring FPA architecture wherein the FPA is operated like a scanning FPA but without optomechanical means. Sensitivity is enhanced beyond that of a true scanning FPA by, for example, using multiple readout bus lines to allow integration times longer than one row time. The sharing reduces circuit multiplicity and frees unit cell real estate to share circuitry and

larger integration capacitance, and to use the otherwise parasitic bus capacitance to further increase capacity. More charge can thus be integrated even though the duty cycle is preset to $1/N$, where $N$ is the number of elements on each common bus.

*Time delay integration scanning FPAs*    While no longer extensively used for staring readouts, SCCDs are used in scanning readouts to incorporate on-focal plane TDI since they have higher dynamic range than FET bucket brigades. Dynamic range >72 dB and as high as 90 dB are typically achieved with high TDI efficacy. Two architectures dominate. In one, the CCD is integrated adjacent to the input circuit in a contiguous unit cell. In the second, the input circuit is segregated from the CCD in a sidecar configuration. The latter offers superior cell-packing density and on-chip signal processing in trade for circuit complexity. Figure 8 shows the schematic circuit for a channel of a scanning readout having capacitive transimpedance amplifier input circuit (discussed earlier), common TDI channel bus, and fill-and-spill[30] input to a sidecar SCCD TDI. This scheme integrates CMOS and CCD processes for much on-chip signal processing in very fine orthoscan pitch.[31]

The readout conversion factor, i.e., volts out per electrons in, for the sidecar CTIA scheme is

$$S_V = \frac{\Delta V}{e^-} = \frac{C_{F/S}}{C_T} A_{V_1} A_{V_2} \frac{q}{C_{out}} \tag{4}$$

where $C_{F/S}$ is the fill-and-spill gate capacitance, $C_T$ is the integration/feedback capacitance, $A_{V_x}$ characterizes the various source follower gains, and $C_{out}$ is the sense node capacitance at the CCD output. The ratio of $C_{F/S}$ to $C_T$ sets a charge gain that allows design-tailoring for managing dynamic range or lowering input-referred noise. High charge-gain yields read noise that is limited by the input circuit and not by the transfer noise[32] of the high-carrier-capacity SCCD.

MOSFET bucket brigades are also used as TDI registers since simpler, all-MOS designs and processes can be used. Advantages include compatibility with standard MOS and CMOS, and capability for external clocking using specific CMOS-compatible clock levels. The latter potential advantage is mitigated in the sidecar TDI scheme by appropriately sizing the SCCD registers and the charge gain to yield the desired CCD clock levels, for example. Disadvantages include higher TDI register noise due to kTC noise being added at each transfer and limited signal excursion.



**FIGURE 8**    Sidecar TDI with capacitive transimpedance amplifier input circuit.

*Output circuits*   Output circuitry is usually kept to a minimum to minimize power dissipation. Circuit design thus tends to focus on the trades between voltage-mode and current-mode output amplifiers, although on-chip signal processing is now at system-on-chip (SoC) level of sophistication, including low-speed A/D conversion, switched-capacitor filtering,[33] and on-chip nonuniformity correction. Voltage-mode outputs offer better S/N performance across a wider range in backgrounds for a given readout transimpedance. Current-mode outputs offer wider bandwidth and better drive capability at higher clock frequencies.

**Detector Interface: Input Circuit**   After the incoming photon flux is converted into a signal by the detector, it is coupled into the readout via a detector interface circuit.[34] Signal input is optical in a monolithic FPA, so signal conditioning is limited. In hybrid FPAs and some composite material monolithics, the signal is injected electrically into the readout. The simplest input schemes offering the highest mosaic densities include direct detector integration (DDI) and direct injection (DI). More complex schemes trade simplicity for input impedance reduction [buffered direct injection (BDI) and capacitive transimpedance amplification (CTIA)], background suppression (e.g., gate modulation), or ultralow read noise with high speed (CTIA). We briefly describe the more popular schemes and their performance. Listed in Table 1 are approximate performance-describing equations for comparing the circuits schematically shown in Fig. 9.

*Direct detector integration*   Direct detector integration (Fig. 9a), also referred to as source follower per detector (SFD), is used at low backgrounds and long frame times (frame rates typically ≤15 Hz in large staring arrays). Photocurrent is stored directly on the detector capacitance, thus requiring the detector to be heavily reverse-biased to maximize dynamic range. The changing detector voltage modulates the gate of a source follower whose drive FET is in the cell and whose current source is common to all the detectors in a column or row. The limited cell area constrains the source followers' drive capability and thus the bandwidth.

The DDI unit cell typically consists of the drive FET, cell enable transistor(s), and reset transistor(s). A detector site is read out by strobing the appropriate row clock, thus enabling the output source follower. The DDI circuit is capable of read noise as low as a few electrons per pixel.

*Direct injection*   Direct injection (Fig. 9b) is perhaps the most widely used input circuit due to its simplicity and high performance. The detector directly modulates the source of a MOSFET. The direct coupling requires that detectors with p-on-n polarity, as is the case with InSb and most photovoltaic LWIR detectors, interface p-type FETs (and vice versa) for carrier collection in the integration capacitor. In surface channel CCDs, the input transistor's drain is virtual, as formed by a fully enhanced well, and often doubles as the integration capacitor.

Practical considerations, including limited charge-handling capacity, constrain the DI input to operation with high-impedance MWIR or limited cutoff ($\lambda_c \leq 9.5$ μm) LWIR detectors. The associated background photocurrent for the applications where direct injection can be used mandates that the DI FET operate subthreshold.[35] The subthreshold gate transconductance, $g_m$, is independent of FET geometry:[36]

$$g_m = \left(\frac{\partial I_D}{\partial V_G}\right)\Bigg|_{V_{DS}=\text{constant}} = \frac{q\left[\eta_{\text{inj}}\left\{I_{\text{photo}} + \frac{V_{\text{det}}}{R_{\text{det}}} - I_{\text{det}_0}(e^{(qV_{\text{det}}/n\det kT)} - 1)\right\}\right]}{nkT} \approx \frac{qI_D}{nkT} \tag{5}$$
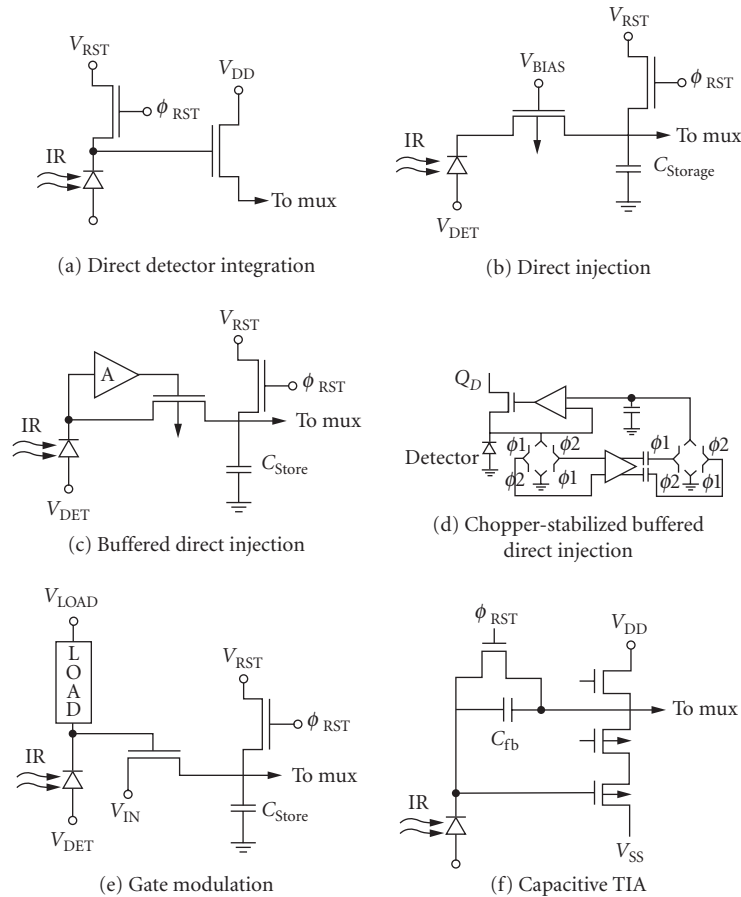
The injection efficiency, $\eta_{\text{inj}}$, of detector current into the DI FET is

$$\eta_{\text{inj, DI}} = \frac{g_m R_{\text{det}}}{1 + g_m R_{\text{det}}}\left[\frac{1}{1 + \dfrac{j\omega C_{\text{det}} R_{\text{det}}}{+ g_m R_{\text{det}}}}\right] \tag{6}$$

where $R_{\text{det}}$ and $C_{\text{det}}$ are the detectors' dynamic resistance and capacitance, respectively. Poor DI circuit bandwidth occurs at low-photon backgrounds due to low $g_m$.

**TABLE 1** Focal Plane Array Performance

| Input Circuit | Percentage of BLIP | Detector Noise | Input-Referred Circuit Noise | Input-Referred MUX Noise | Transimpedance |
|---|---|---|---|---|---|
| Direct Detector Integration | $\dfrac{(\eta A_{det} Q_B \tau_{int})^{1/2}}{\left[\eta A_{det} Q_B \tau_{int} + \dfrac{2kT\tau_{int}}{qR_{det}} + N_{rf}^2 + \dfrac{2kT\tau_{int}}{qR_{int}}\right]^{1/2}}$ | $I_{det}^2 = \left[\dfrac{4KT}{R_{det}} + 2qI_{det}\right]\Delta f + \int^{\Delta f}\left(\dfrac{K_{det}}{f}\right)df$ | $N_{sf} \approx \dfrac{\sqrt{2}}{S_V}\left[\int^{\Delta f} V_n^2(f)\dfrac{(1-\cos 2\pi ft)}{[1+(2\pi fT_D)]}df\right]^{1/2}$ ; $S_V = \left(\dfrac{C_{det}A_V}{q}\right)^{-1}$ | $\sigma_{mux,ir}^2 = \dfrac{1}{A_V^2}kTC_{bus}\Delta f$ | $\left(\dfrac{t_{int}}{C_{det}}\right)A_V$ |
| Direct Injection | $\dfrac{(2qI_{photo}\Delta f)^{1/2}}{(\sigma_{det}^2 + \sigma_{input,ir}^2 + \sigma_{mux,ir}^2)^{1/2}}$ | | | $\sigma_{mux,ir}^2 = \dfrac{1}{\eta_{inj}^2}kTC_{input}\Delta f$ | $\left(\dfrac{t_{int}}{C_{int}}\right)A_V$ |
| Buffered Direct Injection | $\dfrac{(2qI_{photo}\Delta f)^{1/2}}{(\sigma_{det}^2 + \sigma_{input,ir}^2 + \sigma_{mux,ir}^2)^{1/2}}$ | | $\sigma_{input,ir}^2 = \int^{\Delta f}\left[\eta_{noise}^2\left(\dfrac{8}{3}kTg_m + \dfrac{K_{FET}}{f^\alpha}\right) + \Lambda_{amp}^2\langle e_{amp}^2\rangle\right]df$ ; $\eta_{noise} = \dfrac{1+j\omega R_{det}C_{int}}{1+(1+A_V)g_m R_{det} + j\omega R_{det}(1+A_V)C_{int}}$ ; $\Lambda_{amp} = \left(\dfrac{g_m}{R_{det}}\right)\dfrac{(1+j\omega R_{det}C_{det})}{1+(1+A_V)g_m R_{det} + j\omega[C_{det}+(1+A_V)C_{int}]R_{det}}$ | $\sigma_{mux,ir}^2 = \dfrac{1}{\eta_{inj}^2}kTC_{input}\Delta f$ | $\left(\dfrac{t_{int}}{C_{int}}\right)A_V$ |
| Chopper-Stabilized BDI | $\dfrac{(2qI_{photo}\Delta f)^{1/2}}{(\sigma_{det}^2 + \sigma_{input,ir}^2 + \sigma_{mux,ir}^2)^{1/2}}$ | | $\sigma_{input,ir}^2 = \int^{\Delta f}\left[\eta_{noise}^2\left(\dfrac{8}{3}kTg_m\right) + \Lambda_{amp}^2\langle e_{amp}^2\rangle\right]df$ ; $\eta_{noise} = \dfrac{1+j\omega R_{det}C_{int}}{1+(1+A_V)g_m R_{det} + j\omega R_{det}(1+A_V)C_{int}}$ ; $\Lambda_{amp} = \left(\dfrac{g_m}{R_{det}}\right)\dfrac{(1+j\omega R_{det}C_{det})}{1+(1+A_V)g_m R_{det} + j\omega[C_{det}+(1+A_V)C_{int}]R_{det}}$ | $\sigma_{mux,ir}^2 = \dfrac{1}{\eta_{inj}^2}kTC_{input}\Delta f$ | $\left(\dfrac{t_{int}}{C_{int}}\right)A_V$ |
| Gate Modulation (FET Load) | $\dfrac{(2qI_{photo}\Delta f)^{1/2}}{(\sigma_{det}^2 + \sigma_{load}^2 + \sigma_{input,ir}^2 + \sigma_{mux,ir}^2)^{1/2}}$ | | $\sigma_{input,ir}^2 = \int^{\Delta f}\left[\dfrac{1}{A_I^2}\left(2qI_{input} + \dfrac{K_{FET,input}}{f^\alpha}\right)\right]df$ | $\sigma_{mux,ir}^2 = \dfrac{1}{A_{inj}^2}kTC_{input}\Delta f$ | $\left(\dfrac{A_I t_{int}}{C_{int}}\right)A_V$ |
| Capacitive Trans-impedance Amplifier | $\dfrac{\eta A_{det}Q_B\tau_{int}}{\left[\eta A_{det}Q_B\tau_{int} + \dfrac{2kT\tau_{int}}{qR_{det}} + N_{amp,1/f}^2 + N_{amp,white}^2 + N_{load,white}^2\right]^{1/2}}$ | | $N_{amp,1/f} \approx \dfrac{C_{det}K_{amp}\sqrt{2}}{q}\left[\ln\dfrac{5\tau_{int}}{\tau_{amp}}\right]$ ; $N_{amp,white} \approx \dfrac{C_{det}}{q}\sqrt{\dfrac{8}{3}\dfrac{kT}{g_m\tau_{amp}\pi}}$ ; $N_{load,white} \approx \dfrac{C_{det}}{qA_{v,amp}A_V^2}\sqrt{\dfrac{2kT}{C_L}}$ | $I_{mux,ir}^2 = kTC_{input}\Delta f$ | $Z_T = \dfrac{\tau_{int}}{C_T}A_{v,sf}$ ; $C_T = \dfrac{\left[(C_{gd}+C_{gs}+C_{det}) + A_V(C_{fb}+C_{gd})\right]}{A_V}$ |

**33.19**

**FIGURE 9**  Hybrid FPA detector interface circuits.

The injection efficiency varies across an FPA due to FET threshold, detector bias, and detector resistance nonuniformity. Changes in detector current create detector bias shifts since the input impedance is relatively high. In extreme cases a large offset in threshold gives rise to excess detector leakage current and $1/f$ noise, in addition to fixed pattern noise. The peak-to-peak threshold voltage nonuniformity spans the range from ≈1 mV for silicon $p$-MOSFETs to over 125 mV for some GaAs-based readouts.

Depending upon the interface to the multiplexing bus, the noise-limiting capacitance, $C_{input}$, is approximately the integration capacitance or the combined integration and bus capacitance. Some direct-injection cells are thus buffered with a source follower (see Fig. 7). Omitting the source follower reduces the readout transimpedance (due to charge splitting between the integration capacitor and thus bus line capacitance) in trade for larger integration capacitance since more unit-cell real estate is available.

Increasing the pixel density has required a continuing reduction in cell pitch. Figure 10 plots the charge-handling capacity as functions of cell pitch and minimum gate length for representative DI designs using the various minimum feature lengths. Also plotted is the maximum capacity assuming the cell is composed entirely of integration capacitor (225 ÅiO$_2$). A 27-μm DI cell, fabricated in 1.25-μm CMOS, thus had similar cell capacity as an earlier 60-μm DI cell in 3-μm CMOS. Limitations on cell real estate, operating voltage, and the available capacitor dielectrics nevertheless
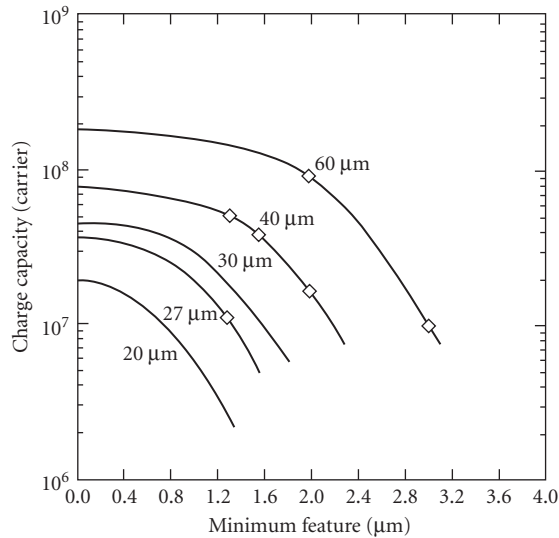
**FIGURE 10**   Direct injection charge-handling capacity versus cell pitch for standard CMOS processes.

dictate maximum integration times that are often shorter than the total frame time. This duty cycling equates to degradation in detective quantum efficiency.

*Buffered direct injection*    A significant advantage of the source-coupled input is MOSFET noise suppression. This suppression is implied in the $\eta_{\text{BLIP}}$ expression shown in Table 1. When injection efficiency is poor, however, MOSFET noise becomes a serious problem along with bandwidth. These deficiencies are ameliorated via buffered direct injection (BDI),[37] wherein a feedback amplifier with open-loop gain $-A_v$ (Fig. 9c) is added to the DI circuit. The buffering increases injection efficiency to near-unity, increases bandwidth by orders of magnitude, and suppresses the DI FET noise.

BDI has injection efficiency

$$\eta_{\text{inj}} \cong \frac{g_m R_{\text{det}}(1+A_V}{1+g_m R_{\text{det}}(1+A_v)+j\omega R_{\text{det}}[(1+A_v)C_{\text{amp}}+C_{\text{det}}]} \tag{7}$$

where $C_{\text{amp}}$ is the Miller capacitance of the amplifier. Circuit bandwidth is maximized by lowering the amplifiers' Miller capacitance to provide detector-limited frequency response that is lower than that possible with DI by the factor $(1+A_V)$.

The noise margin of the BDI circuit is superior to DI, even though two additional noise sources associated with the feedback amplifier are added. The dominant circuit noise stems from the drive FET in the amplifier. The noise power for frequencies less than $1/(2\pi R_{\text{det}}C_{\text{det}})$ is directly proportional to the detector impedance. Amplifier noise is hence a critical issue with low impedance (<1 M$\Omega$) detectors including long wavelength photovoltaics operating at temperatures above 80 K.

*Chopper-stabilized buffered direct injection*    The buffered direct injection circuit has high 1/$f$ noise with low-impedance detectors. While the MOSFET 1/$f$ noise can be suppressed somewhat by reverse-biasing the detectors to the point of highest resistance, detector 1/$f$ noise may then dominate. Other approaches include enlarging MOSFET gate area, using MOS input transistors in the lateral bipolar mode, or using elaborate circuit techniques such as autozeroing and chopper stabilization. Chopper stabilization is useful if circuit real estate is available, as in a scanning readout. Figure 9d shows a block diagram schematic circuit of chopper-stabilized BDI.

Chopper stabilization refers to the process of commutating the integrating detector node between the inverting and noninverting inputs of an operational amplifier having open-loop gain, $A_V$. This chopping process shifts the amplifier's operating frequency to higher frequencies where the amplifier's noise is governed by white noise, not $1/f$ noise. At chopping frequencies $f_{\text{chop}} \gg f_k$, the equivalent low-frequency input noise of the chopper amplifier is equal to the original amplifier white-noise component.[38] The amplifier's output signal is subsequently demodulated and filtered to remove the chopping frequency and harmonics. This scheme also reduces the input offset nonuniformity by the reciprocal of the open-loop gain, thereby generating uniform detector bias. Disadvantages include high circuit complexity and the possibility of generating excess detector noise via clock feedthrough-induced excitation of traps, particularly with narrow bandgap photovoltaic detectors.

*Gate modulation*   Signal processing can be incorporated in a small unit cell by using a gate-modulated input structure (c.f. MOSFET load gate modulation in Fig. 9e).[39] The use of an MOSFET as an active load device, for example, provides dynamic range management via automatic gain control and user-adjustable background pedestal offset since the detector current passes through a load device with resistance $R_{\text{LOAD}}$. The differential gate voltage applied to the input FET varies for a change in photocurrent, $\Delta I_{\text{photo}}$, as

$$\Delta V_G = R_{\text{LOAD}} \eta_{\text{inj, DI}} \Delta I_{\text{photo}} \qquad (8)$$

The current injected into the integration capacitor is

$$I_{\text{input}} = g_m R_{\text{LOAD}} \eta_{\text{inj, DI}} \Delta I_{\text{photo}} \qquad (9)$$

The ratio of $I_{\text{input}}$ to $I_{\text{photo}}$ is the current gain, $A_I$, which is

$$A_I = \frac{g_m}{g_{m,\text{LOAD}}} \eta_{\text{inj, DI}} \qquad (10)$$

The current gain can self-adjust by orders of magnitude depending on the total detector current. Input-referred read noise of tens of electrons has thus been achieved with high-impedance SWIR detectors at low-photon backgrounds. The same circuit has also been used at LWIR backgrounds with LWIR detectors having adequate impedance for good injection efficiency.

The current gain expression suggests a potential shortcoming for imaging applications since the transfer characteristic is nonlinear, particularly when the currents in the load and input FETs differ drastically. In conjunction with tight specifications for threshold uniformity, pixel functionality can be decreased, dynamic range degraded, and imagery dominated by spatial noise. The rms fractional gain nonuniformity (when operating subthreshold) of the circuit is approximately

$$\frac{\Delta A_I}{A_I} = \frac{q\sigma_{VT}}{n_{\text{FET}} kT} \qquad (11)$$

where $\sigma_{VT}$ is the rms threshsold nonuniformity. At 80 K, state-of-the-art $\sigma_{VT}$ of 0.5 mV for a $128 \times 128$ FPA, and $n = 1$, the minimum rms nonuniformity is $\approx 7$ percent.

*Capacitive transimpedance amplifier (CTIA)*   Many CTIAs have been successfully demonstrated. The most popular approach uses a simple CMOS inverter[40] for feedback amplification (Fig. 9f). Others use a more elaborate differential amplifier. The two schemes differ considerably with respect to open-loop voltage gain, bandwidth, power dissipation, and cell real estate. The CMOS inverter-based CTIA is more attractive for high-density arrays. The latter is sometimes preferred for scanning or *Z*-hybrid applications where real estate is available primarily to minimize power dissipation.[41]

In either case, photocurrent is integrated directly onto the feedback capacitor of the transimpedance amplifier. The minimum feedback capacitance is set by the amplifier's Miller capacitance and defines the maximum circuit transimpedance. Since the Miller capacitance can be made very small (<5 fF), the resulting high transimpedance yields excellent margin with respect to

downstream system noise. The transimpedance degrades when the circuit is coupled to large detector capacitances, so reducing pixel size serves to minimize read noise and the circuits' attractiveness will continue to increase in the future.

The CTIA allows extremely small currents to be integrated with high efficiency and tightly regulated detector bias. The amplifier open-loop gain, $A_{V,\text{amp}}$, ranges from as low as on the order of ten to higher than several thousand for noncascoded inverters, and many thousands for cascoded inverter and differential amplifier designs. The basic operating principle is to apply the detector output to the inverting input of a high-gain CMOS differential amplifier operated with capacitive feedback. The feedback capacitor is reset at the detector sampling rate. The noise equivalent input voltage of the amplifier is referred to the detector impedance, just as in other circuits.

The CTIA's broadband channel noise sets a lower limit on the minimum achievable read noise, is the total amplifier white noise, and can be approximated for condition of large open-loop gain by

$$N^2_{kTC,\text{channel}} = \frac{kTC_{\text{fb}}}{q^2} \left[ \frac{C_{\text{det}} + C_{\text{fb}}}{C_L + \dfrac{C_{\text{fb}}C_{\text{det}}}{C_{\text{fb}} + C_{\text{det}}}} \right] \tag{12}$$

where $C_{\text{fb}}$ is the feedback capacitance including the Miller capacitance and integration capacitance and $C_L$ is the output load capacitance. This expression provides an intuitive formula for minimizing noise: detector capacitance must be low (i.e., minimize detector shunting capacitance which reduces closed-loop gain) and output capacitance high (i.e., limit bandwidth). Of the three amplifier noise sources listed in Table 1, amplifier $1/f$ noise is often largest. For this reason, the CMOS inverter-based CTIA has best performance with $p$-on-$n$ detectors and $p$-MOSFET amplifier FET due to the lower $1/f$ noise.

## 33.5  PERFORMANCE: FIGURES OF MERIT

In the early days of infrared technology, detectors were characterized by the noise equivalent power (NEP) in a 1-Hz bandwidth. This was a good specification for single detectors, since their performance is usually amplifier limited. The need to compare detector technologies for application to different geometries and the introduction of FPAs having high-performance on-board amplifiers and small parasitics necessitated normalization to the square root of the detector area for comparing S/N. R. C. Jones[42] thus introduced detectivity ($D^*$), which is simply the reciprocal of the normalized NEP and has units cm-$\sqrt{\text{Hz}}$/W (or Jones).

While $D^*$ is well-suited for specifying infrared detector performance, it can be misleading to the uninitiated since the $D^*$ is highest at low background. An LWIR FPA operating at high background with background-limited performance (BLIP) S/N can have a $D^*$ that is numerically lower than for a SWIR detector having poor S/N relative to the theoretical limit. Several figures of merit that have hence proliferated include other ways of specifying detectivity: e.g., thermal $D^*$ ($D^*_{\text{th}}$), blackbody $D^*$($D^*_{\text{bb}}$), peak $D^*$ ($D^*_{\lambda\text{pk}}$), percentage of BLIP (%BLIP or $\eta_{\text{BLIP}}$), and noise equivalent temperature difference (NE$\Delta T$). Since the final output is an image, however, the ultimate figure of merit is how well objects of varying size are detected and resolved in the displayed image. The minimum resolvable temperature (MRT) is thus a key benchmark. These are briefly discussed in this section.

### Detectivity ($D^*$)

$D^*$ is the S/N ratio normalized to the electrical bandwidth and detector area. In conjunction with the optics area and the electrical bandwidth, it facilitates system sensitivity estimation. However, $D^*$ can be meaningless unless the test conditions, including magnitude and spectral distribution of the flux source (e.g., blackbody temperature), detector field-of-view, chopping frequency (lock-in amplifier),

background temperature, and wavelength at which the measurement applies. $D^*$ is thus often quoted as "blackbody," since the spectral responsivity is the integral of the signal and background characteristics convolved with the spectral response of the detector. $D^*_{bb}$ specifications are often quantified for a given sensor having predefined scene temperature, filter bandpass, and cold shield $f/\#$ using a generalized expression.

Peak detectivity is sometimes preferred by detector engineers specializing in photon detectors. The background-limited peak detectivity for a photovoltaic detector is

$$D^*_{\lambda pk} = \sqrt{\frac{\eta}{2Q_B}} \frac{\lambda_{pk}}{hc} \tag{13}$$

and refers to measurement at the wavelength of maximum spectral responsivity. For detector-limited scenarios, such as at higher operating temperatures or longer wavelengths (e.g., $\lambda_c > 12$ µm at operating temperature less than 78 K or $\lambda_c > 4.4$ µm at >195 K), the peak detectivity is limited by the detector and not the photon shot noise. In these cases the maximum detector-limited peak $D^*$ in the absence of excess bias-induced noise (both $1/f$ and shot noise) is

$$D^*_{\lambda pk} = \frac{\eta q}{2} \sqrt{\frac{R_0 A}{kT}} \frac{\lambda}{hc} \tag{14}$$

The $R_0 A$ product of a detector thus describes detector quality even though other parameters may actually be more relevant for FPA operation.

## Percentage of BLIP

Whereas $D^*$ compares the performance of dissimilar detectors, FPA designers often need to quantify an FPA's performance relative to the theoretical limit at a specific operating background. Percentage of BLIP, $\eta_{BLIP}$, is one such parameter and is simply the ratio of photon noise to composite FPA noise

$$\eta_{BLIP} = \left( \frac{N^2_{PHOTON}}{N^2_{PHOTON} + N^2_{FPA}} \right)^{1/2} \tag{15}$$

## NE$\Delta T$

The NE$\Delta T$ of a detector represents the temperature change, for incident radiation, that gives an output signal equal to the rms noise level. While normally thought of as a system parameter, detector NE$\Delta T$ and system NE$\Delta T$ are the same except for system losses (conservation of radiance). NE$\Delta T$ is defined:

$$NE\,\Delta T = \upsilon_n \left( \frac{\partial T}{\partial Q} \right) \Big/ \left( \frac{\partial V_s}{\partial Q} \right) = \upsilon_n \frac{\Delta T}{\Delta V_s} \tag{16}$$

where $\upsilon_n$ is the rms noise and $\Delta V_S$ is the signal measured for the temperature difference $\Delta T$. It can be shown that

$$NE\,\Delta T = \left( \tau_o C_{T\lambda} \eta_{BLIP} \sqrt{N_c} \right)^{-1} \tag{16a}$$

where $\tau_o$ is the optics transmission, $C_{T\lambda}$ is the thermal contrast from Fig. 1, and $N_c$ is the number of photogenerated carriers integrated for one integration time, $t_{int}$:

$$N_c = \eta A_{det} t_{int} Q_B \tag{16b}$$

The distinction between an integration time and the FPA's frame time must be noted. It is often impossible at high backgrounds to handle the large amount of carriers generated over frame times compatible with standard video frame rates. The impact on system $D^*$ is often not included in the FPA specifications provided by FPA manufacturers. This practice is appropriate for the user to assess relative detector quality, but must be coupled with usable FPA duty cycle, read noise, and excess noise to give a clear picture of FPA utility. Off-FPA frame integration can be used to attain a level of sensor sensitivity that is commensurate with the detector-limited $D^*$ and not the charge-handling-limited $D^*$.

The inability to handle a large amount of charge nevertheless is a reason why the debate as to whether LWIR or MWIR operation is superior is still heated. While the LWIR band should offer order-of-magnitude higher sensitivity, staring readout limitations often reduce LWIR imager sensitivity to below that of competing MWIR cameras. However, submicron photolithography, alternative dielectrics, and refinements in readout architectures are ameliorating this shortfall and LWIR FPAs having sensitivity superior to MWIR counterparts are available. Figure 11 shows the effect on high quantum efficiency FPA performance and compares the results to PtSi at TV-type frame rate. The figure illustrates BLIP and measured NE $\Delta T$s versus background temperature for several spectral bands assuming a $640 \times 480$ DI readout multiplexer (27-µm pixel pitch and ≈1-µm-minimum
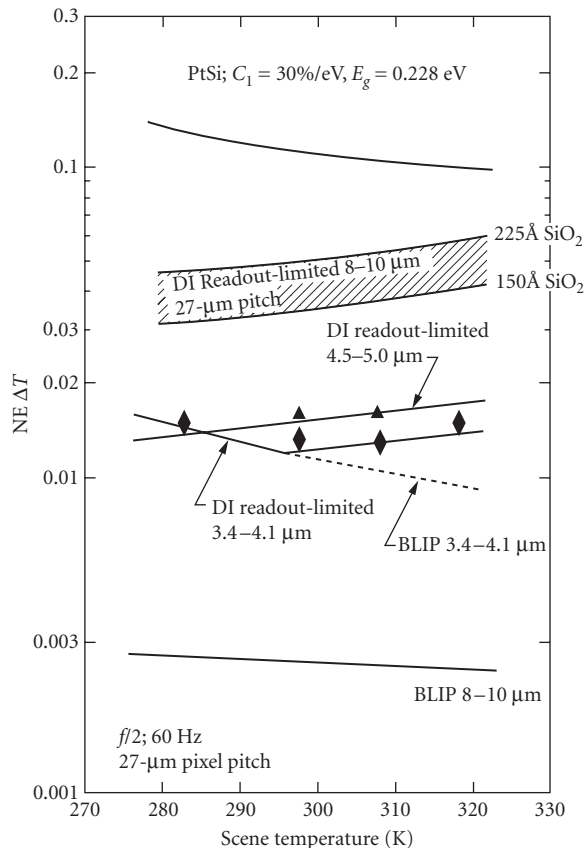


**FIGURE 11**  NE $\Delta T$ versus background temperature for several prominent spectral bands.

feature) is hybridized to high-quantum-efficiency MWIR and LWIR detectors. Though the device has large charge-handling capacity, there is large shortfall in the predicted LWIR FPA performance relative to the BLIP limit. The measured MWIR FPA performance values, as shown by the data points, are in good agreement with the predicted trends.

*Spatial noise*    Estimation of IR sensor performance must include a treatment of spatial noise that occurs when FPA nonuniformities cannot be compensated correctly. This requires consideration of cell-to-cell response variations. Mooney et al.[43] comprehensively discussed the origin of spatial noise. The total noise determining the sensitivity of a staring array is the composite of the temporal noise and the spatial noise. The spatial noise is the residual nonuniformity $U$ after application of nonuniformity compensation, multiplied by the signal electrons $N$. Photon noise, equal to $\sqrt{N}$, is the dominant temporal noise source for the high infrared background signals for which spatial noise is significant (except for TE-cooled or uncooled sensors). The total noise equivalent temperature difference is

$$\text{Total NE}\,\Delta T = \frac{\sqrt{N+U^2N^2}}{\dfrac{\partial N}{\partial T}} = \frac{\sqrt{1/N+U^2}}{\dfrac{1}{N}\dfrac{\partial N}{\partial T}} \tag{17}$$

where $\partial N/\partial T$ is the signal change for a 1 K source temperature change. The denominator, $(\partial N/\partial T)/N$, is the fractional signal change for a 1 K source temperature change. This is the relative scene contrast due to $C_{T\lambda}$ and the FPA's transimpedance.

The dependence of the total NE$\Delta T$ on residual nonuniformity is plotted in Fig. 12 for 300 K scene temperature, two sets of operating conditions, and three representative detectors: LWIR HgCdTe, MWIR HgCdTe, and PtSi. Operating case A maximizes the detected signal with $f/1.4$ optics, 30-Hz frame rate, and 3.4 to 5.0-μm passband. Operating case B minimizes the solar influence by shifting the passband to 4.2 to 5.0 μm and trades off signal for the advantages of lighter, less expensive optics ($f/2.0$) at 60-Hz frame rate. Implicit in the calculations are charge-handling capacities of 30 million e⁻ for MWIR HgCdTe, 100 million e⁻ for LWIR HgCdTe, and 1 million for PtSi. The sensitivity at the lowest nonuniformities is independent of nonuniformity and limited by the
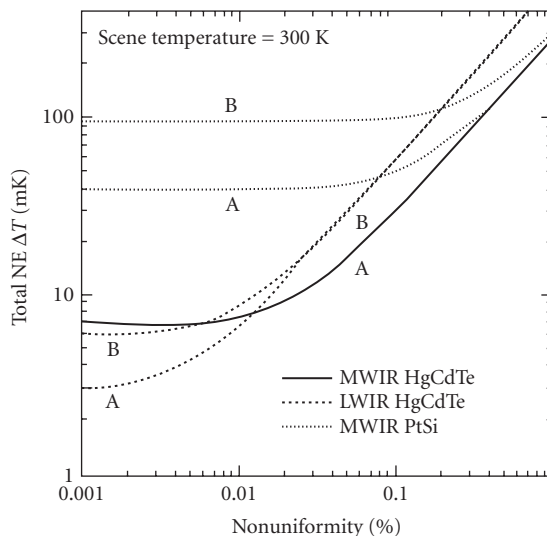


**FIGURE 12**    Total NE$\Delta T$ versus nonuniformity at 300 K scene temperature.

shot noise of the detected signal. The LWIR sensitivity advantage is achieved only at nonuniformities less than 0.01 percent, which is comparable to that achieved with buffered input circuits. At the reported direct-injection MWIR HgCdTe residual nonuniformity of 0.01 to 0.02 percent, the total NE$\Delta T$ is about 0.007 K, which is comparable to the MWIR BLIP limit. At the reported PtSi residual nonuniformity of 0.05 percent with direct detector integration, total NE$\Delta T$ is higher at 0.04K, but exceeds the BLIP limit for the lower quantum efficiency detectors.

## Minimum Resolvable Temperature

The minimum resolvable temperature (MRT) is often the preferred figure of merit for imaging infrared sensors. MRT is a function of spatial resolution and is defined as the signal-to-noise ratio required for an observer to resolve a series of standard four-bar targets. While many models exist due to the influence of human psycho-optic response, a representative formula[44] is

$$\mathrm{MRT}(f_s, T_{\mathrm{SCENE}}) = \frac{2\mathrm{SNR}_T \mathrm{NE}\,\Delta T(T_{\mathrm{SCENE}})}{\mathrm{MRT}(f_s)} \left[ \frac{f_S^2 \Delta x \Delta y}{L\tau_{\mathrm{eye}} f_{\mathrm{frame}} N_{\mathrm{OS}} N_{\mathrm{SS}}} \right]^{1/2} \qquad (18)$$

where $f_s$ is the spatial frequency in cycles/radian, a target signal-to-noise ratio ($\mathrm{SNR}_T$) of five is usually assumed, the MTF describes the overall modulation transfer function including the optics, detector, readout, and the integration process, $\Delta x$ and $\Delta y$ are the respective detector subtenses in mRad, $\tau_{\mathrm{eye}}$ is the eye integration time, $f_{\mathrm{frame}}$ is the display frame rate, $N_{\mathrm{OS}}$ is the overscan ratio, $N_{\mathrm{SS}}$ is the serial scan ratio, and $L$ is the length-to-width ratio of a bar chart (always set to 7). While the MRT of systems with temporal noise-limited sensitivity can be adequately modeled using the temporal NE$\Delta T$, scan noise in scanned system and fixed pattern noise in staring cameras requires that the MRT formulation be appropriately modified.

Shown in Fig. 13 are BLIP (for 70 percent quantum efficiency) MRT curves at 300 K background temperature for narrow-field-of-view (high-resolution) sensors in the MWIR and LWIR spectral bands. Two LWIR curves are included to show the impact of matching the diffraction-limited blur
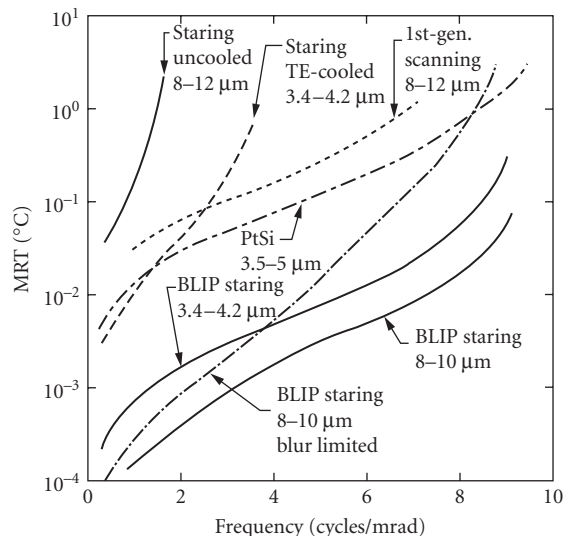


**FIGURE 13**   BLIP MRT for representative staring FPA configurations in the various bands.

to the pixel pitch versus 2× oversampling of the blur. The latter case commonly arises, for example, when the LWIR FPA is miniaturized to minimize die size for enhancing yield and, for hybrid FPAs, alleviating thermal expansion mismatch. Also included for comparison are representative curves for first-generation scanning, staring uncooled, staring TE-cooled and staring PtSi sensors assuming 0.1, 0.1, 0.05, and 0.1 K NE$\Delta T$s, respectively. Theoretically, the staring MWIR sensors have order of magnitude better sensitivity while the staring LWIR bands have two orders of magnitude better sensitivity than the first-generation sensor. In practice, due to charge-handling limitations, an LWIR sensor has only slightly better MRT than the MWIR sensor. The uncooled sensor is useful for short-range applications such as a driver's aid in modern automobiles; the TE-cooled sensor provides longer range than the uncooled, but less than the high-density PtSi-based cameras.

## 33.6   CURRENT STATUS AND FUTURE TRENDS

### Status

After over three decades of ongoing development, today's second-generation infrared focal plane arrays have typically 1000 times more pixels and up to 10 times higher sensitivity than first-generation devices. FPA format is consequently now set by application need, rather than a technological barrier. Nevertheless, there is ongoing motivation for fully achieving theoretically limited performance, especially at elevated operating temperatures. Development is hence continuing in the form of third-generation FPA technology. While specifications for third-generation FPAs encompass a broad range of needs, common objectives require overcoming recurring practical limits with respect to sensitivity, frame rate, power dissipation, multispectral capability, and cost. The common methodology going forward, regardless of specific mission requirements, is to dramatically increase on-FPA functionality via system-on-chip integration. While second-generation technology was largely driven by defense-oriented R&D funding, it is likely that third-generation technology will more directly leverage emerging commercial foundry capability for 3D-IC assembly; this emerging commercial interest in 3D-IC integration should dramatically lower infrared FPA cost while further improving FPA performance.

Figure 14 summarizes the typical performance of the most prominent detector technologies. The figure, a plot of the $D_{th}^*$ (300 K, 0° field-of-view) versus operating temperature, clearly shows the performance advantage that the intrinsic photovoltaics have over the other technologies. Thermal detectivity is used here to compare the various technologies for equivalent NE$\Delta T$ irrespective of wavelength. While the extrinsic silicon detectors offer very high sensitivity, high producibility, and very long cutoff wavelengths, the very low operating temperature is often prohibitive. Also shown is the relatively low and slightly misleading detectivity of PtSi, which is offset by its
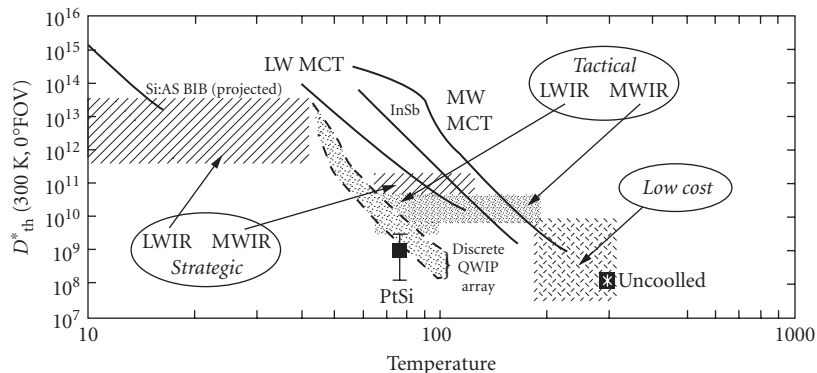


**FIGURE 14**   Comparison of photon detector $D_{th}^*$ (300 K, 0°) for varous IR technologies for equivalent NE$\Delta T$.

**FIGURE 15**   Thermal image of a man holding a match detected by the 640 × 480 MOS imager. (*Courtesy of Sarnoff*).

excellent array uniformity (i.e., array performance is commensurate with best diode performance). Thermal imaging achieved with a Sarnoff 640 × 480 PtSi FPA is shown in Fig. 15, an image free of the artifacts often plaguing competing detector technologies. Table 2 further summarizes the characteristics of monolithic and hybrid PtSi FPAs with IR-CCD, CSD, and MOS silicon multiplexers developed at the peak of PtSi FPA interest. In addition to the pixel size and fill factor, this table also shows the process design rules, maximum charge signal, $Q_{max}$, the reported noise equivalent temperature (NE $\Delta T$) for operation with specific $f/\#$ optics, the associated company, and the pertinent references for that era.

**TABLE 2**   Representative Staring PtSi FPAs

| Type of FPA | Pixel Size ($\mu m^2$) | Fill Factor | Design Rules ($\mu m$) | $Q_{max} \times 10^6$ ($e^-$/p) | NE$\Delta T$ (K) | NE$\Delta T$ $f/\#$ | Year | Company | References |
|---|---|---|---|---|---|---|---|---|---|
| 320 × 244 IT-CCD | 40 × 40 | 44 | 2.0 | 1.4 | 0.04 | 1.4 | 1988 | Sarnoff | 46 |
| 680 × 480 MOS | 24 × 24 | 38 | 1.5 | 1.5 | 0.06 | 1.0 | 1991 | | 47 |
| 324 × 487 IT-CCD | 42 × 21 | 42 | 1.5 | 0.25 | 0.10 | 1.0 | 1988 | NEC | 48 |
| 648 × 487 IT-CCD | 21 × 21 | 40 | 1.3 | 1.5 | 0.10 | 1.0 | 1991 | | 49 |
| 256 × 244 IT-CCD | 31.5 × 25 | 36 | 1.8 | 0.55 | 0.07 | 1.8 | 1989 | Loral | 50 |
| 512 × 512 IT-CCD | | | | | | | | Fairchild | |
| 640 × 486 IT-CCD | 25 × 25 | 54 | 1.2 | | | | | Kodak | |
|   noninterl. 4-port | | | | 0.23 | 0.15 | 2.8 | 1990 | | 51 |
|   interlaced 1-port | | | | 0.55 | <0.1 | 2.8 | 1991 | | |
| 512 × 512 CSD | 26 × 20 | 39 | 2.0 | 0.7 | 0.1 | 1.5 | 1987 | Mitsubishi | 52 |
| | | 71 | 1.2 | 2.9 | 0.033 | 1.5 | 1992 | | 53 |
| 1040 × 1040 CSD 4-port | 17 × 17 | 53 | 1.5 | 1.6 | 0.1 | 1.2 | 1991 | | 45 |
| 400 × 244 hybrid | 24 × 24 | 84 | 2.0 | 0.75 | 0.08 | 1.8 | 1990 | Hughes | 54 |
| 640 × 488 hybrid 4-point | 20 × 20 | 80 | 2.0 | 0.75 | 0.1 | 2.0 | 1991 | | 55 |

Similar in performance at cryogenic temperatures, InSb and HgCdTe have comparable array size and pixel yield at MWIR cutoff wavelengths. Wavelength tunability and high radiative efficiency, however, have often made HgCdTe the preferred material because the widest possible bandgap semiconductor can be configured and thus the highest possible operating temperature achieved for a given set of operating conditions. The associated cooling and system power requirements can thus be optimally distributed.

FPA costs are currently very similar for all the second-generation FPA technologies. Though it is often argued that FPA cost for IR cameras will be irrelevant once it reaches a certain minimum production volume, nevertheless the key determinants as to which FPA technology becomes ubiquitous in the coming decade are availability and cost.

## Future Trends and Technology Directions

The 1980s saw the maturation of PtSi and the emergence of HgCdTe and InSb as producible MWIR detector materials. Many indicators pointed to the 1990s being the decade that IR FPA technology would enter the consumer marketplace, but penetration did not actually occur until a decade later. Figure 16 shows the chronological development of IR FPAs including monolithic and hybrid technologies. Specifically compared is the development of various hybrids (primarily MWIR) to PtSi, the pace-setting technology with respect to array size. The hybrid FPA data includes Pb-salt, HgCdTe, InSb, and PtSi devices. This database suggests that monolithic PtSi led all other technologies with respect to array size by about 2 years and clearly shows the thermal mismatch barrier confronted by hybrid FPA developers in the mid-1980s.

In addition to further increases in pixel density to $>10^{16}$ pixels, several trends are clear. Future arrays will have much more on-chip signal processing, need less cooling, have higher sensitivity (particularly intrinsic LWIR FPAs), and offer multispectral capability. If the full performance potential of the uncooled technologies is realized, either the microbolometer arrays or, less likely, the pyroelectric arrays will capture the low-cost markets. It is not unreasonable that the uncooled arrays may obsolete "low-cost" PtSi, QWIP, and HIP FPAs, and render the intrinsic TE-cooled developments inconsequential. To improve hybrid reliability, alternative detector substrate materials including silicon along with alternative readout materials will become sufficiently mature to begin monolithic integration of the intrinsic materials with highest radiative performance. True optoelectronic FPAs consisting of IR sensors with optical output capability may be developed for reducing
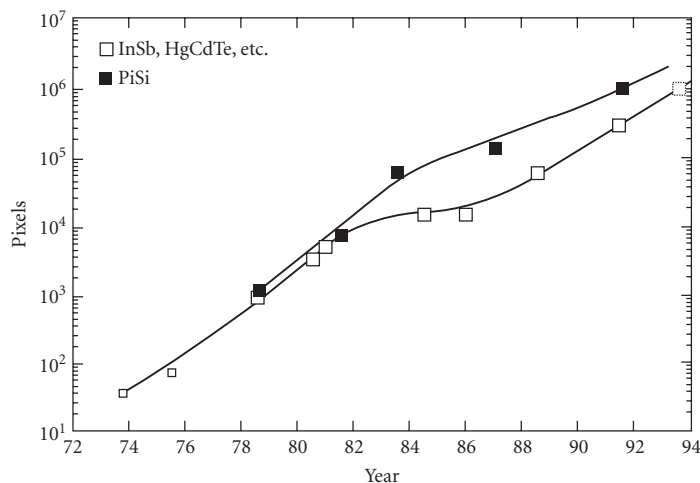


**FIGURE 16**   Chronological development of IR FPAs.
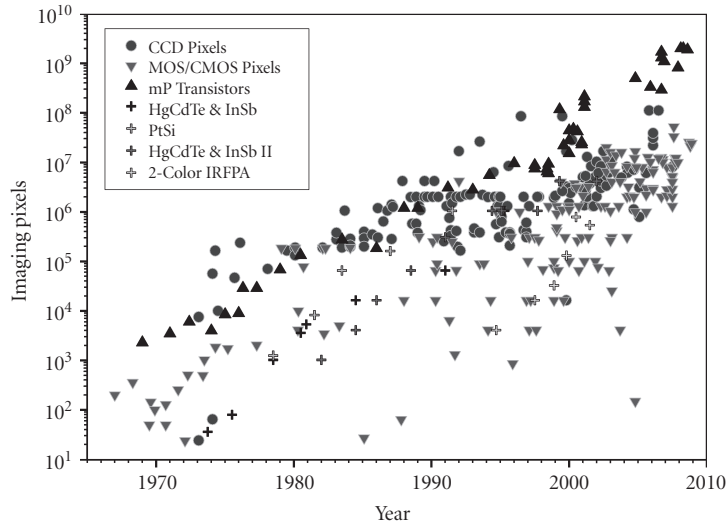
**FIGURE 17**   Integrated Circuit Chronology.

thermal loading and improving immunity to noise pickup. Availability of inexpensive, commercial devices is imminent along with the development of IR neural networks for additional signal processing capability.

In conclusion, it is likely instructive to compare the development of infrared sensors with both visible imaging sensors and other commercial integrated circuits, including semiconductor memory and microprocessors. All these products commonly share the benefits derived from Moore's law.[56] Fig. 17 is such a chronology showing notable devices of all types. Early infrared devices tended to develop at a pace only a few years behind the overlying trend known as Moore's law. Multicolor sensors initially developed at a rapid pace since the infrastructure was already in place. All infrared devices lag visible sensor development, which is driven by consumer demand. The largest visible sensors now boast about 100 million pixels; these foreshadow the size of upcoming infrared sensors once reliability issues and packaging costs are fully contained.

## 33.7   REFERENCES

1. W. P. McCracken, "CCDing in the Dark," *IEEE Spectrum.* (1992).

2. P. R. Norton, "Infrared Image Sensors," *Opt. Eng.* **30:**11 (1991).

3. A. Rogalski and J. Piotrowski, "Intrinsic Infrared Detectors," *Progress in Quantum Electronics* 12, Pergamon Press, 1988, pp. 2–3.

4. S. B. Stetson, D. B. Reynolds, M. G. Stapelbroek, and R. L. Stermer, "Design and Performance of Blocked-Impurity-Band Detector Focal Plane Arrays," *SPIE Proceedings,* vol. 686 (1986).

5. M. D. Petroff, G. Stapelbroek, and W. A. Kleinhans, "Solid State Photomultiplier," U.S. Patent No. 4,586,068 (1983).

6. B. F. Levine, K. K. Choi, C. G. Bethea, J. Walker, and R. J. Malik, *Appl. Phys. Lett.* **50:**1092 (1987).

7. C. S. Wu et al., "Novel GaAs/AlGaAs Multiquantum-Well Schottky Junction Device and Its Photovoltaic LWIR Detection," *IEEE Trans. Electron Devices,* **ED-39:**2 (1992).

8. J. Cooper, *Rev. Sci. Instrum.* **33:**92 (1962).

9. C. Hanson, H. Beratan, R. Owen, M. Corbin, and S. McKenney, "Uncooled Thermal Imaging at Texas Instruments," *SPIE Proceedings,* vol. 1735, 1992.

10. D. H. Pommerrenig, "Extrinsic Silicon Focal Plane Array," *SPIE Proceedings,* vol. 443, 1983.

11. (*a*) W. F. Kosonocky, "Review of Infrared Image Sensors with Schottky-Barrier Detectors," *Optoelectronics— Devices and Technologies,* vol. 6, no. 2, December 1991, pp. 173–203. (*b*) W. F. Kosonocky, "State-of-the-Art in Schottky-Barrier IR Image Sensors," *SPIE Proceedings,* vol. 1681, Orlando, Fla., 1992.

12. Private communications with N. A. Foss from Sensors and Systems Center, Honeywell, Inc., Bloomington, Minn.

13. C. G. Roberts, "HgCdTe Charge Transfer Focal Planes," *SPIE Proceedings,* vol. 443, 1983.

14. M. D. Gibbons et al., "Status of IrSb Charge Injection Device (CID) Detection Technology," *SPIE Proceedings,* vol. 443, 1983.

15. M. H. White et al., "Characterization of Surface CCD Image Arrays at Low Light Levels," *IEEE J. Solid-State Circuits,* vol. SC-9, 1974, pp. 1–12.

16. D. J. Sauer, F. V. Shallcross, F. L. Hsueh, G. M. Meray, P. A. Levine, H. R. Gilmartin, T. S. Villani, B. J. Esposito, and J. R. Tower, "640 × 480 MOS PtSI IR Sensor," *SPIE Proceedings,* vol. 1540, 1991, pp. 285–296.

17. L. J. Kozlowski et al., "Comparison of Passive and Active Pixel Schemes for CMOS Visible Imagers," *SPIE* 3360, 1998.

18. W. F. Kosonocky, T. S. Villani, F. V. Shallcross, G. M. Meray, and J. J. O'Neill, III, "A Schottky-Barrier Image Sensor with 100% Fill Factor," *SPIE Proceedings,* vol. 1308, 1990, pp. 70–80.

19. M. Denda, M. Kimata, S. Iwade, N. Yutani, T. Kondo, and N. Tsubouchi, "4 × 4096-Element SWIR Multispectral Focal Plane Array," *SPIE Proceedings,* vol. 819–824, 1987, pp. 279–286.

20. K. Chow, J. P. Rode, D. H. Seib, and J. D. Blackwell, "Hybrid Infrared Focal Plane Arrays," *IEEE Trans. Electron Devices* **ED-29**(1) (January, 1982).

21. E. R. Gertner, W. E. Tennant, J. D. Blackwell, and J. P. Rode, "HgCdTe on Sapphire—A New Approach to Infrared Detector Arrays," *J. Cryst. Growth* **72:**465 (1985).

22. E. R. Gertner, *Ann. Rev. Mater. Sci.* **15:**303–328 (1985).

23. E. R. Fossum, "Infrared Readout Electronics," *SPIE Proceedings,* vol. 1684 (1992).

24. D. F. Barbe, "Imaging Devices Using the Charge-Coupled Concept," *Proc. IEEE* **63**(1) (1975).

25. P. Felix, M. Moulin, B. Munier, J. Portmann, and J.-P. Reboul, "CCD Readout of Infrared Hybrid Focal Plane Arrays," *IEEE Trans. Electron Devices* **ED-27**(1) (1980).

26. S. T. Baier, "Complementary Heterostructure (CHFET) Readout Technology for Infrared Focal Plane Arrays," *SPIE Proceedings,* vol. 1684 (1992).

27. R. Sahai, R. L. Pierson, R. J. Anderson, E. H. Martin, E. A. Sover, and J. Higgins, "GaAs CCD's with Transparent (ITO) Gates for Imaging and Optical Signal Processing," *IEEE Electron Device Lett.* **EDL-4** (1983).

28. L. J. Kozlowski and R. E. Kezer, "2 × 64 GaAs Readout for IR FPA Application," *SPIE Proceedings,* vol. 1684 (1992).

29. J. S. Bugler and P. G. A. Jespers, "Charge Pumping in MOS Devices," *IEEE Trans, on Electron Devices* **ED-16:**3 (1969).

30. M. F. Tompsett, "Surface Potential Equilibration Method of Setting Charge in Charge-Coupled Devices," *IEEE Trans. Electron Devices* **ED-22:**6 (1975).

31. L. J. Kozlowski, K. Vural, W. E. Tennant, R. E. Kezer, and W. E. Kleinhans, "10 × 132 CMOS/CCD Readout with 25 μm Pitch and On-Chip Signal Processing Including CDS and TDI," *SPIE Proceedings,* vol. 1684 (1992).

32. M. F. Tompsett, "The Quantitative Effects of Interface States on the Performance of Charge-Coupled Devices," *IEEE Trans. Electron Devices* **ED-20:**1 (1973).

33. P. W. Bosshart, "A Multiplexed Switched Capacitor Filter Bank," *IEEE Journal Solid-State Circuits,* **SC-15:**6 (1980).

34. W. S. Chan, "Detector-Charge-Coupled Device (CCD) Interface Methods," *SPIE Proceedings,* vol. 244 (1980).

35. R. M. Swanson and J. D. Meindl, "Ion-Implanted Complementary MOS Transistors in Low-Voltage Circuits," *IEEE Journal of Solid-State Circuits* **SC-7:**2 (1972).

36. R. Troutman and S. N. Chakravarti, "Subthreshold Characteristics of Insulated-Gate Field-Effect Transistors," *IEEE Trans. Circuit Theory* **CT-20:**6 (1973).

37. N. Bluzer and R. Stehlik, "Buffered Direct Injection of Photocurrents into Charge-Coupled Devices," *IEEE Journal of Solid-State Circuits* **SC-13:**1 (1978).

38. C. C. Enz, E. A. Vittoz, and F. Krummenacher, "A CMOS Chopper Amplifier," *IEEE Journal of Solid-State Circuits* **SC-22:**3 (1987).

39. S. G. Chamberlain and J. P. Y. Lee, "A Novel Wide Dynamic Range Silicon Photodetector and Linear Imaging Array," *IEEE Trans. Electron Devices* **ED-31:**2 (1984).

40. F. Krummenacher, E. Vittoz, and M. DeGrauwe, "Class AB CMOS Amplifier for Micropower SC Filters," *Electron. Lett.* **17:**13 (1981).

41. E. Vittoz and J. Fellrath, "CMOS Analog Integrated Circuits Based on Weak Inversion Operation," *IEEE Journal Solid State Circuits* **SC-12:**3 (1977).

42. R. D. Hudson, *Infrared System Engineering,* John Wiley and Sons, 1969.

43. J. M. Mooney et al., "Responsivity Nonuniformity Limited Performance of Infrared Staring Cameras," *Opt. Eng.* **28:**1151 (1989).

44. D. L. Shumaker, J. T. Wood, and C. R. Thacker, *FLIR Performance Handbook,* DCS Corporation, Alexandria, Va. (1988).

45. N. Yutani, M. Kimata, H. Yagi, J. Nakanishi, S. Nagayoshi, and N. Tubouchi, "1040 × 1040 Element PtSi Schottky-Barrier IR Image Sensor," IEDM, Washington, D.C., 1991.

46. T. S. Villani, W. F. Kosonocky, F. V. Shallcross, J. V. Groppe, G. M. Meray, J. J. O'Neill, III, and B. J. Esposito, "Construction and Performance of a 320 × 244-Element IR-CCD Imager with PtSi SBDs," *SPIE Proceedings,* vol. 1107–01, 1989, pp. 9–21.

47. D. J. Sauer, F. V. Shallcross, F. L. Hsueh, G. M. Meray, P. A. Levine, H. R. Gilmartin, T. S. Villani, B. J. Esposito, and J. R. Tower, "640 × 480 MOS PtSi IR Sensor," *SPIE Proceedings,* vol. 1540, 1991, pp. 285–296.

48. K. Konuma, N. Teranishi, S. Tohyama, K. Masubuchi, S. Yamagata, T. Tanaka, E. Oda, Y. Moriyama, N. Takada, and N. Yoshioka, "324 × 487 Schottky-Barrier Infrared Imager," *IEEE Trans. Electron Devices,* **37**(3):629–635 (1990).

49. K. Konuma, S. Tohyama, A. Tanabe, K. Masubuchi, N. Teranishi, T. Saito, and T. Muramatsu, "A 648 × 487 Pixel Schottky-Barrier Infrared CCD Image Sensor," *1991 ISSCC Digest of Tech. Papers,* 1991, pp. 156–157.

50. H. Elabd, Y. Abedini, J. Kim, M. Shih, J. Chin, K. Shah, J. Chen, F. Nicol, W. Petro, J. Lehan, M. Duron, M. Manderson, H. Balopole, P. Coyle, P. Cheng, and W. Shieh, "488 × 512 and 244 × 256-Element Monolithic PtSi Schottky IR Focal Plane Arrays," *SPIE Proceedings,* vol. 1107–29, presented at *SPIE Aerospace Sensor Symposium,* Orlando, Fla., March 1989.

51. E. T. Nelson, K. Y. Wong, S. Yoshizumi, D. Rockafellow, W. DesJardin, M. Elzinga, J. P. Lavine, T. J. Tredwell, R. P. Khosla, P. Sorlie, B. Howe, S. Brickman, and S. Refermat, "Wide Field of View PtSi Infrared Focal Plane Array," *SPIE Proceedings,* vol. 1308, 1990, pp. 36–44.

52. M. Kimata, M. Denda, N. Yutani, S. Iwade, and N. Tsubouchi, "A 512 × 512-Element PtSi Schottky-Barrier Infrared Image Sensor," *IEEE J. Solid-State Circuits,* vol. SC-22, no. 6, 1987, pp. 1124–1129.

53. H. Yagi, N. Yutani, S. Nagayoshi, J. Nakanishi, M. Kimata, and N. Tsubouchi, "Improved 512 × 512 IR CSD with Large Fill Factor and Large Saturation Level," *SPIE Proceedings,* vol. 1685–04, 1992.

54. J. Edwards, J. Gates, H. Altin-Mees, W. Connelly, and A. Thompson, "244 × 400 Element Hybrid Platinum Silicide Schottky Focal Plane Array," *SPIE Proceedings,* vol. 1308, 1990, pp. 99–100.

55. J. L. Gates, W. G. Connelly, T. D. Franklin, R. E. Mills, F. W. Price, and T. Y. Wittwer, "488 × 640-Element Hybrid Platinum Silicode Schottky Focal Plane Array," *SPIE Proceedings,* vol. 1540, *Infrared Technology XVII,* 1991, pp. 262–273.

56. G. E. Moore, "Cramming More Components onto Integrated Circuits," Electronics Magazine **38:**8, 1965.